

# Ferroptotic stress promotes the accumulation of pro-inflammatory proximal tubular cells in maladaptive renal repair

Shintaro Ide<sup>1†</sup>, Yoshihiko Kobayashi<sup>2†</sup>, Kana Ide<sup>1</sup>, Sarah A Strausser<sup>1</sup>, Koki Abe<sup>1</sup>, Savannah Herbek<sup>1</sup>, Lori L O'Brien<sup>3</sup>, Steven D Crowley<sup>1</sup>, Laura Barisoni<sup>1,4</sup>, Aleksandra Tata<sup>2</sup>, Purushothama Rao Tata<sup>2,5,6</sup>, Tomokazu Souma<sup>1,5\*</sup>

<sup>1</sup>Division of Nephrology, Department of Medicine, Duke University School of Medicine, Durham, United States; <sup>2</sup>Department of Cell Biology, Duke University School of Medicine, Durham, United States; <sup>3</sup>Department of Cell Biology and Physiology, University of North Carolina at Chapel Hill, Chapel Hill, United States; <sup>4</sup>Department of Pathology, Duke University School of Medicine, Durham, United States; <sup>5</sup>Regeneration Next, Duke University, Durham, United States; <sup>6</sup>Duke Cancer Institute, Duke University School of Medicine, Durham, United States

**Abstract** Overwhelming lipid peroxidation induces ferroptotic stress and ferroptosis, a non-apoptotic form of regulated cell death that has been implicated in maladaptive renal repair in mice and humans. Using single-cell transcriptomic and mouse genetic approaches, we show that proximal tubular (PT) cells develop a molecularly distinct, pro-inflammatory state following injury. While these inflammatory PT cells transiently appear after mild injury and return to their original state without inducing fibrosis, after severe injury they accumulate and contribute to persistent inflammation. This transient inflammatory PT state significantly downregulates glutathione metabolism genes, making the cells vulnerable to ferroptotic stress. Genetic induction of high ferroptotic stress in these cells after mild injury leads to the accumulation of the inflammatory PT cells, enhancing inflammation and fibrosis. Our study broadens the roles of ferroptotic stress from being a trigger of regulated cell death to include the promotion and accumulation of proinflammatory cells that underlie maladaptive repair.

**\*For correspondence:**

tomokazu.souma@duke.edu

†These authors contributed equally to this work

**Competing interests:** The authors declare that no competing interests exist.

**Funding:** See page 26

**Received:** 20 March 2021

**Preprinted:** 23 March 2021

**Accepted:** 17 July 2021

**Published:** 19 July 2021

**Reviewing editor:** Gregory G Germino, National Institutes of Health, United States

© Copyright Ide et al. This article is distributed under the terms of the [Creative Commons Attribution License](https://creativecommons.org/licenses/by/4.0/), which permits unrestricted use and redistribution provided that the original author and source are credited.

## Introduction

Acute kidney injury (AKI) afflicts 1.2 million hospitalized patients annually in the US; 20–50% of AKI survivors progress to chronic kidney disease (CKD), increasing their risk for dialysis-dependency, cardiovascular events, and mortality (*Chawla et al., 2014; Lewington et al., 2013; Strausser et al., 2018*). Other than general supportive care, there are no targeted therapies to treat AKI or to prevent AKI to CKD transition. A better understanding of the molecular events underpinning the AKI to CKD transition is needed to develop therapeutic strategies to interrupt this devastating disease process.

Clinical and preclinical studies have identified damage to proximal tubular (PT) epithelial cells after severe AKI as a critical mechanism driving transition to CKD (*Strausser et al., 2018; Chawla et al., 2011; Liu et al., 2017; Cippà et al., 2018; Ferenbach and Bonventre, 2015; Humphreys, 2018*). PT cells are most severely affected by acute ischemic and toxic injuries due to their high metabolic and energy-intensive transporter activities required to maintain normal homeostasis of body fluids (*Ferenbach and Bonventre, 2015; Humphreys, 2018; Gewin, 2018*). In the renal

repair process, damaged PT cells adopt heterogeneous molecular states (Kiritani *et al.*, 2020). They reactivate genes normally active during renal development (Rudman-Melnick *et al.*, 2020; Kang *et al.*, 2016; Kumar *et al.*, 2015), alter their dependency on metabolic fuels (Legouis *et al.*, 2020), change their morphology, and proliferate to replenish the areas of denuded epithelium in the proximal tubule (Ferenbach and Bonventre, 2015; Witzgall *et al.*, 1994). When the initial damage to kidneys is mild, PT cells subsequently return to their original state by redifferentiation, with resolution of inflammation and fibrosis (Ferenbach and Bonventre, 2015; Kiritani *et al.*, 2020; Rudman-Melnick *et al.*, 2020; Legouis *et al.*, 2020; Witzgall *et al.*, 1994; Berger *et al.*, 2014; Kusaba *et al.*, 2014). However, if damage is more extensive, prolonged, or recurrent, the damaged cells fail to redifferentiate, leading to persistent inflammation, fibrosis, and eventual cell death. The molecular pathways that govern proximal tubular heterogeneity and cell fate during failed renal repair after severe injury are poorly understood. This knowledge gap prevents the development of therapies based on underlying disease mechanisms.

One of the critical pathways involved in AKI pathogenesis and proximal tubular cell death is ferroptosis, a distinct non-apoptotic form of regulated cell death (Stockwell *et al.*, 2017; Dixon *et al.*, 2012; Yang *et al.*, 2014; Kagan *et al.*, 2017; Doll *et al.*, 2017; Alim *et al.*, 2019; Zhao *et al.*, 2020; Linkermann *et al.*, 2014). An imbalance between the generation of lipid peroxides and their detoxification induces overwhelming accumulation of lipid peroxides (ferroptotic stress), triggering ferroptosis (Stockwell *et al.*, 2017; Alim *et al.*, 2019). The glutathione/glutathione peroxidase 4 (GPX4) axis is the central defense pathway to prevent ferroptotic stress and ferroptosis (Stockwell *et al.*, 2017; Dixon *et al.*, 2012; Yang *et al.*, 2014; Friedmann Angeli *et al.*, 2014). Global genetic deletion of *Gpx4* in mice causes renal tubular epithelial death and acute kidney injury, identifying renal tubular epithelial cells as one of the cell types most vulnerable to ferroptotic stress (Friedmann Angeli *et al.*, 2014). Moreover, reduced glutathione and NADPH availability further render ischemia-reperfusion injured kidneys vulnerable to ferroptotic stress (Strausser *et al.*, 2018; Nezu *et al.*, 2017). Accumulating evidence suggests that pharmacological inhibition of ferroptotic cell death ameliorates AKI severity and excess ferroptotic stress has been linked to failed renal repair in patients, suggesting a new therapeutic target (Zhao *et al.*, 2020; Linkermann *et al.*, 2014; Friedmann Angeli *et al.*, 2014; Wenzel *et al.*, 2017). Interestingly, recent evidence suggests that molecular regulators of necroptosis, another form of regulated cell death, contribute to disease pathogenesis by additional pathways independent of their well-documented roles in triggering cell death (Daniels *et al.*, 2017; Moriwaki and Chan, 2016; Moriwaki *et al.*, 2014). However, it is still not clear whether ferroptotic stress has additional roles in the pathogenesis of AKI and its sequelae beyond the induction of ferroptotic cell death and loss of functional tubular cells.

Here, using complementary single-cell transcriptomic and mouse genetic approaches, we identify the role of a molecularly distinct, damage-associated, PT cell state that is dynamically and differentially regulated during successful versus failed repair. Furthermore, we provide mechanistic evidence that ferroptotic stress in PT cells enhances this damage-associated state, in addition to triggering cell death, thereby promoting failed renal repair and the AKI-to-CKD transition.

## Results

### Tubular epithelial cells exhibit heterogeneous molecular states after severe injury

To identify cellular mechanisms that promote maladaptive repair after severe kidney injury, we first developed and optimized mouse models for ‘successful’ versus ‘failed’ renal repair after ischemia-reperfusion-induced injury (IRI). This was achieved by extending renal ischemic times from 20 min for successful recovery to 30 min for failed recovery (Figure 1—figure supplement 1 and Figure 1—figure supplement 2). After mild injury, histologic examination showed that inflammation and macrophage accumulation resolved within 21 days (ischemic time 20 min; Figure 1—figure supplement 1, D and E). By contrast, after severe injury there was progressive epithelial damage and fibrosis, and the accumulation of F4/80+ macrophages persisted around the damaged epithelial cells for at least 6 months (ischemic time 30 min; Figure 1—figure supplement 1, D and E; and Figure 1—figure supplement 2E).

We used this failure-to-repair model (unilateral IRI, ischemic time 30 min) to generate a single-cell transcriptome map of failed renal repair (**Figure 1A**). Kidneys were harvested at 6 hr and 1, 7, and 21 days after IRI. High-quality transcriptome data from a total of 18,258 cells from injured kidneys (IRI) and homeostatic uninjured kidneys (Homeo) were obtained (**Figure 1, B and C**). Using a Seurat integration algorithm that normalizes data and removes potential batch effects (**Stuart et al., 2019; Hafemeister and Satija, 2019**), we integrated the transcriptome data from each condition and performed unsupervised clustering analysis of the integrated dataset. Uniform manifold approximation and projection (UMAP) resolved 21 separate clusters, representing distinct cell types (**Figure 1B; Figure 1—figure supplement 3B and Figure 1—figure supplement 4A**). The cellular identity of each cluster was determined based on known cell-type-specific markers (**Park et al., 2018; Ransick et al., 2019**). We successfully identified known cell-type-specific damage-induced genes such as *Havcr1* (kidney injury molecule-1, KIM1), *Krt8* (keratin 8), *Krt20* (keratin 20), and *Lcn2* (neutrophil gelatinase-associated lipocalin, NGAL) selectively in ischemia-reperfusion-injured (IRI) kidneys, but not in homeostatic uninjured control kidneys (**Figure 1—figure supplement 3C**), (**Liu et al., 2017; Ichimura et al., 2008; Paragas et al., 2011**).

Based on the cell clustering and gene expression patterns, we noticed that there are at least three epithelial cell states (homeostatic normal, activated, and dedifferentiated cells) in our dataset (See **Figure 1A**, right panel). Homeostatic normal cells express high expression of ‘anchor’ genes involved in normal cell function and identity (**Figure 1—figure supplement 3, B and C**). Most of the tubular epithelial cells from IRI kidneys robustly expressed damage-induced genes (ex. *Havcr1*, *Krt8*, *Krt20*, *Lcn2*), indicating they are in activated states (**Figure 1—figure supplement 3C**). These activated cells and homeostatic cells were grouped in the same cluster because they both highly express anchor genes characteristic for normal tubular epithelial states and functions (**Figure 1, B and C; Fig. Figure 1—figure supplement 3C**). However, we also identified additional damage-associated tubular epithelial clusters (**Figure 1C**, arrowheads; DA-PT, DA-TAL, and DA-DCT) that had lost or reduced expression of ‘normal’ mature epithelial cell marker genes but highly expressed damage-induced genes (**Figure 1—figure supplement 3, B and C, Figure 1A**).

Among these damage-associated epithelial cell clusters, we found a damage-associated proximal tubular cell state (See DA-PT cluster), which shows reduced homeostatic gene expression (ex. *Lrp2*, *Slc34a1*, *Hnf4a*, and *Acsm2*) and enrichment for genes associated with both renal development and kidney injury in human and mouse (ex. *Cdh6*, *Sox9*, *Sox4*, *Cited2*, *Vcam1*, *Vim*, and *Havcr1*; **Figure 1D**, and **Figure 1—figure supplement 5B and Figure 1—figure supplement 6A**), (**Combes et al., 2019a; Famulski et al., 2012; Adam et al., 2017**). Moreover, gene ontology enrichment analyses of this cellular population revealed proinflammatory molecular signatures and enriched expression of chemokines and cytokines such as *Cxcl2*, *Cxcl1*, *Ccl2*, and *Spp1* (**Figure 1—figure supplement 5B,D and E**). Reduced expression of *Hnf4a*, which is a transcription factor essential for the maturation of PT cells (**Marable et al., 2018; Marable et al., 2020**), and other homeostatic genes and upregulation of *Cdh6*, which is selectively expressed in immature proximal tubule progenitors in development and is essential for renal epithelialization (**Marable et al., 2020; Cho et al., 1998; Mah et al., 2000**), suggest that the cells in this cluster (DA-PT) are in a less differentiated cell state (**Figure 1D and Figure 1—figure supplement 6A**), (**Marable et al., 2020**). Then, we compared the transcriptional signature of this damage-associated PT cell state with previously published neonatal kidney single-cell RNA seq data (GSE94333, **Figure 1—figure supplement 7, A and B**), (**Adam et al., 2017**). The top 100 genes enriched in immature early PT cells in neonatal kidneys were mainly expressed in this damage-associated PT cell state (DA-PT, **Figure 1—figure supplement 7, C and D**). These analyses support our notion that the cells in the DA-PT cluster are in a dedifferentiated inflammatory state.

Among the damage-induced genes expressed in this dedifferentiated inflammatory PT cell state, we focused on the enrichment of *Sox9* and *Vcam1* (**Figure 1D**, See DA-PT cluster, arrowheads). Recent single-nucleus transcriptomic profiling of mouse IRI-kidneys identified vascular cell adhesion molecule 1 (VCAM1) as a marker of non-repairing proximal tubular cell state (**Kirita et al., 2020**), and *Vcam1* induction has been observed in multiple forms of human kidney diseases, including allograft rejection (**Hauser et al., 1997**). SRY-box9 (SOX9) is an essential transcription factor for successful renal repair after acute ischemic and toxic insults (**Kang et al., 2016; Kumar et al., 2015**) and is involved in the development of multiple organs, including mouse and human kidneys (**Reginensi et al., 2011**). SOX9 contributes to tissue repair processes by conferring stemness,

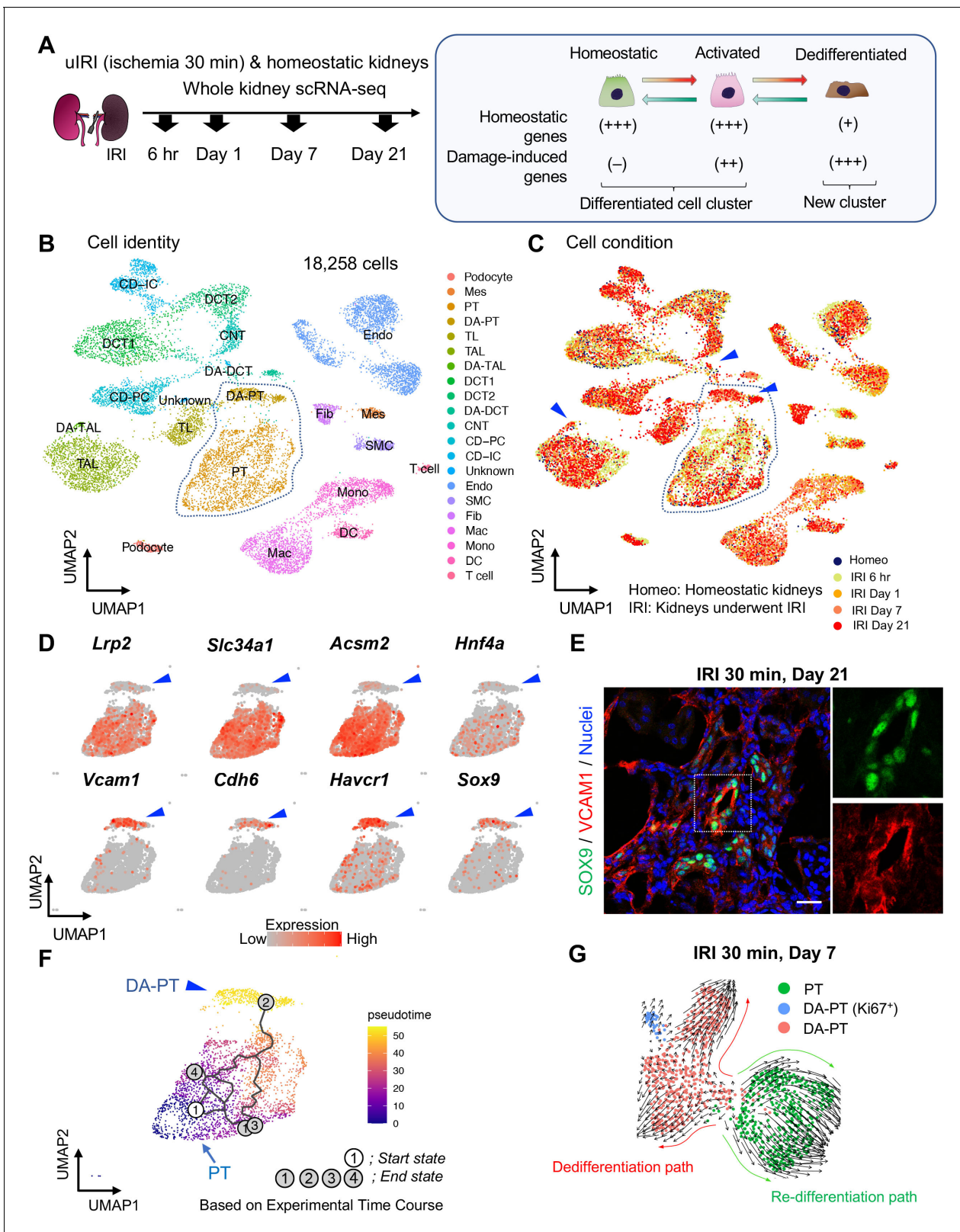


**Figure 1.** Single-cell RNA sequencing (scRNA-seq) identifies dynamic cellular state transitions of tubular epithelial cells after severe IRI. (A) Drop-seq strategy. uIRI, unilateral IRI. A schematic illustration of epithelial cell states is shown. (B) and (C) Integrated single-cell transcriptome map. Unsupervised clustering identified 21 distinct clusters in the UMAP plot. Arrowheads indicate damage-associated tubular epithelial cells. The dotted area (PT cell clusters; PT and DA-PT) was used for the downstream analyses in (D)–(G). (D) UMAP plots showing the expression of indicated genes in PT cell clusters  
*Figure 1 continued on next page*

Figure 1 continued

(PT and DA-PT in (B)). Differentiated/mature PT cell markers: *Lrp2* (megalin), *Slc34a1* (sodium-dependent phosphate transporter 2a, NaPi2a), *Acsm2* (acyl-coenzyme A synthetase), and *Hnf4a* (hepatocyte nuclear factor 4 $\alpha$ ); and damage-induced genes: *Vcam1* (vascular adhesion molecule 1), *Cdh6* (cadherin 6), *Havcr1* (kidney injury molecule-1, KIM1), *Sox9* (Sry-box 9). Arrowheads; DA-PT. (E) Immunostaining for SOX9 and VCAM1 using post-severe IRI kidneys on day 21. Scale bar: 20  $\mu$ m. (F) Pseudotime trajectory analysis of proximal tubular cells (PT and DA-PT clusters) that underwent IRI. A region occupied with cells from 6 hr after post-IRI was set as a starting state. (G) RNA velocity analysis of PT clusters (PT and DA-PT) from post-IRI kidneys on day 7. Cells in PT clusters from IRI day 7 dataset was extracted for the analysis. The arrows indicate predicted lineage trajectories. PT, proximal tubule; DA-PT, damage-associated PT; TL, thin limb; TAL, thick ascending limb; DA-TAL, damage-associated TAL; DCT, distal convoluted tubule; DA-DCT, damage-associated DCT; CNT, connecting tubule; CD, collecting duct (P, principal cells, IC, intercalated cells); Mes, mesangial cells; Endo, endothelial cells; SMC, smooth muscle cells; Fib, fibroblasts; Mac, macrophages; Mono, monocytes; DC, dendritic cells.

The online version of this article includes the following figure supplement(s) for figure 1:

**Figure supplement 1.** Characterization of severe and mild unilateral IRI models.

**Figure supplement 2.** Severe IRI leads to cystic and atrophic kidneys 6 months after severe IRI.

**Figure supplement 3.** scRNA-seq identifies major cell types in homeostatic and post-IRI kidneys.

**Figure supplement 4.** UMAP plots show the expression pattern of anchor genes in homeostatic and post-IRI kidneys.

**Figure supplement 5.** Damage-associated PT cells show an inflammatory transcriptional signature.

**Figure supplement 6.** Severe IRI reduces expressions of proximal tubular differentiation markers.

**Figure supplement 7.** Comparative analyses of damage-associated PT cells and neonatal proximal tubular cells.

**Figure supplement 8.** Trajectory analyses predict lineage hierarchy from differentiated mature PT cells to damage-associated PT cells.

plasticity, and regenerative capacity (Kang et al., 2016; Kumar et al., 2015; Roche et al., 2015; Kadaja et al., 2014; Furuyama et al., 2011; Tata et al., 2018). Our single-cell RNA-sequencing (scRNA-seq) data revealed that *Sox9* was most robustly induced in damage-associated PT cells compared to other tubular epithelial cells (DA-PT, Figure 1—figure supplement 5C). To validate this finding, we performed immunofluorescence for SOX9 and VCAM1 in histological sections of kidneys with failed repair. SOX9 nuclear accumulation was observed in VCAM1<sup>+</sup> proximal tubular cells (Figure 1E). High expression of *Sox9* and *Vcam1* suggests a potential role of this damage-associated PT cell state both in adaptive and maladaptive renal repair in a context-dependent manner, such as ranging severity of injury.

To understand the lineage hierarchy of PT cell states, we analyzed PT cells from differentiated and damage-associated PT cell clusters (PT and DA-PT in Figure 1B) using two algorithm tools (Monocle 3 and Velocyto) that allow the computational prediction of cell differentiation trajectories (Cao et al., 2019; La Manno et al., 2018). By placing each cell from the entire dataset in pseudotime we observed a predicted differentiation trajectory originating from PT to DA-PT (Figure 1F and Figure 1—figure supplement 8, A and B). We then performed RNA velocity analysis, which predicts the cell state trajectory based on the ratio between unspliced and spliced mRNA expressions, for these two PT cell states from the post-IRI dataset on day 7. Our RNA velocity analysis showed two trajectories running in opposite directions from the middle of the cluster, a position where genes associated with tubular maturation and damage are both not highly expressed (Figure 1G and Figure 1—figure supplement 8C). One projects toward the area with high levels of damage-induced genes (dedifferentiation path to damage-associated PT cell state) and the other toward the area with high levels of maturation-associated genes (redifferentiation path to differentiated PT cell state). Our computational analyses suggest the potential existence of cellular plasticity at this stage (Day 7 post-IRI; Figure 1G and Figure 1—figure supplement 8C).

## Proximal tubular cells dynamically alter their cellular states after acute kidney injury

To determine the temporal dynamics of damage-associated PT cell state in adaptive and maladaptive repair and validate the computational analyses, we performed expression analyses of multiple marker genes for this PT cell state in successful and failed renal repair processes. Quantitative RT-PCR analyses for *Sox9*, *Cdh6*, and *Vcam1* genes confirmed the transient induction of these genes and resolution after mild ischemic injury (20 min ischemia, Fig. 2B), but persistently elevated expression after severe ischemic injury (30 min) through 21 days after injury (Figure 2B). Using immunofluorescence and in situ hybridization, we observed more VCAM1<sup>+</sup> and *Cdh6*<sup>+</sup> tubular epithelial cells in IRI kidneys after 30 min than 20 min ischemia (Figure 2C). The number of SOX9-positive cells was

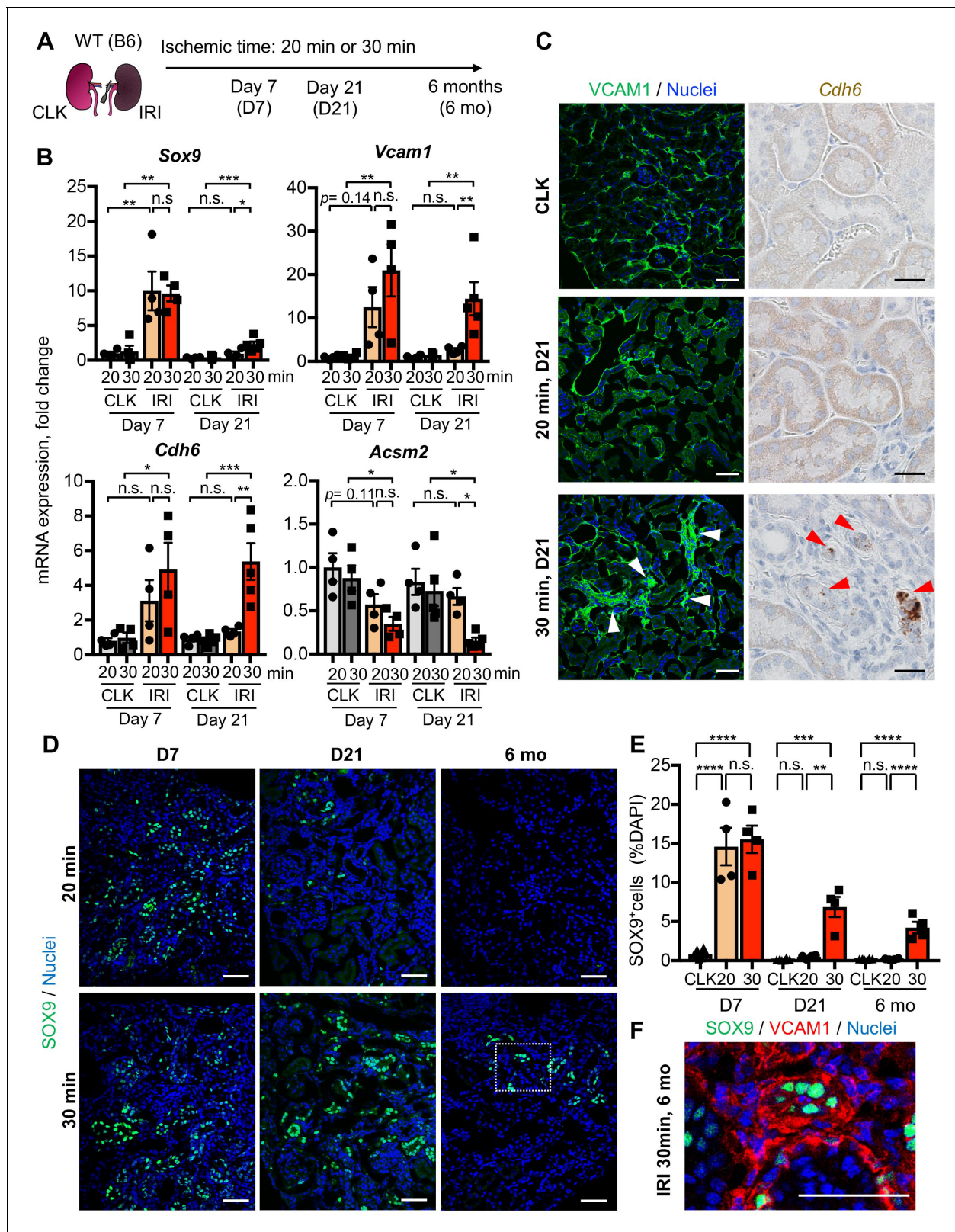


**Figure 2.** Damage-associated PT cells emerge transiently after mild injury but persist after severe injury. (A) Experimental workflow for the mild and severe IRI models. Left kidneys from wild-type (WT) C57BL/6J (B6) mice were subjected to mild (20 min) and severe (30 min) ischemia (unilateral IRI, uIRI). Contralateral kidneys (CLK) were used as controls. (B) Real-time PCR analyses of indicated gene expression. Whole kidney lysates were used. N = 4–5. (C) Expression analyses of VCAM1 and *Cdh6* using post-IRI kidneys on day 21. Immunostaining for VCAM1 revealed clusters of VCAM1<sup>high</sup> tubular cells. (D) Immunostaining for SOX9 and Nuclei in post-IRI kidneys at Day 7, Day 21, and 6 months. (E) Quantification of SOX9<sup>+</sup> cells (%DAPI) in post-IRI kidneys at Day 7, Day 21, and 6 months. (F) Immunostaining for SOX9, VCAM1, and Nuclei in post-IRI kidneys at 6 months. Figure 2 continued on next page

Figure 2 continued

epithelial cells. In situ hybridization (ISH) was used to detect *Cdh6* gene expression on kidney sections. (D) Immunostaining for SOX9 in mild (20 min) and severe (30 min) IRI kidneys collected at indicated time points (day 7, day 21, and 6 months after IRI). (E) Quantification of SOX9<sup>+</sup> cells over the DAPI<sup>+</sup> area. Note that SOX9<sup>+</sup> cells persist after severe IRI up to 6 months after IRI (30 for 30 min ischemia). In contrast, they disappear after a transient appearance in post-mild IRI kidneys (20 for 20 min ischemia). N = 4–8. (F) Immunostaining for SOX9 and VCAM1 (6 months post-severe IRI kidneys, dotted area in D). Scale bars, 20  $\mu$ m in (C, *Cdh6*), and 50  $\mu$ m (C, VCAM1, D and F). \* $p$  < 0.05; \*\* $p$  < 0.01; \*\*\* $p$  < 0.001; \*\*\*\* $p$  < 0.0001, one-way ANOVA with post hoc multiple comparisons test. n.s., not significant.

The online version of this article includes the following figure supplement(s) for figure 2:

**Figure supplement 1.** Comparative analyses of mild and severe IRI identify distinct temporal dynamics of damage-associated PT cells.

similarly increased between kidneys with mild and severe IRI on day 7 compared to baseline (**Figure 2**, D and E). Confocal imaging showed that most of the SOX9-positive cells co-express VCAM1 (**Figure 2—figure supplement 1, B and C**). Notably, SOX9 expression was reduced to baseline level in the kidneys that underwent mild injury while it persisted up to 6 months after severe IRI (**Figure 2**, D and E). We observed clusters of SOX9<sup>+</sup>VCAM1<sup>+</sup> cells in the remaining parenchyma at 6 months post-severe IRI, but not in the post mild-IRI kidneys (**Figure 2F** and **Figure 2—figure supplement 1, B and C**). In accordance with the hypothesis that severe IRI injury is associated with increased signature of damage-associated PT cell state, there was a reduction of homeostatic gene expressions (*Acs2* and *Slc34a1*) and the number of fully differentiated PT cells, which have high lotus tetragonolobus lectin (LTL)-binding (**Figure 2B** and **Figure 1—figure supplement 6, B-D**), (**Marable et al., 2020**). This finding is in line with a clinical correlation between low expression of *ACSM2B*, the human ortholog of *Acs2*, and reduced renal function in patients with CKD (**Ledo et al., 2015**). Collectively, these data support the emergence and accumulation of damage-associated PT cells after severe injury but their return to a homeostatic state after mild injury.

To further characterize the dynamic changes and plasticity of proximal tubular cell state, we employed a *CreERT2* allele of *Sox9*, a highly enriched gene in the damage-associated PT cell state (DA-PT, **Figure 1—figure supplement 5C**), combined with *Rosa26*<sup>tdTomato</sup> reporter to carry out lineage tracing (**Figure 3A**). In this mouse line (*Sox9*<sup>CreERT2</sup>; *Rosa26*<sup>tdTomato</sup>), tamoxifen administration permanently labels the *Sox9*-lineage cells with the tdTomato fluorescent reporter and provides the spatial information of the cells with a history of *Sox9* expression. On day 21, we found that severe ischemia (30 min) induces more robust accumulation of *Sox9*-lineage-labeled cells than mild ischemic injury (20 min) in the cortex and outer medulla of the IRI-kidneys (**Figure 3**, B and C). Approximately 25% percent of *Sox9*-lineage cells that underwent severe IRI were positive for VCAM1 on day 21, suggesting that part of *Sox9*-lineage cells did not fully redifferentiate after severe injury (**Figure 3**, D and E; 30 min). In contrast, only a few *Sox9*-lineage cells that underwent mild injury were VCAM1 positive at this time, indicating successful redifferentiation (**Figure 3**, D and E; 20 min). These results are consistent with the temporal dynamics of SOX9 and VCAM1 immunostaining results (**Figure 2—figure supplement 1**). Taken together, our data suggest that loss of plasticity and impaired redifferentiation of damage-associated PT cells underlie the failed renal repair/regeneration process (**Figure 3F**).

## Damage-associated PT cells create a proinflammatory milieu with renal myeloid cells

While an initial inflammatory response is critical for tissue repair, uncontrolled persistent inflammation underlies organ fibrosis (**Ferenbach and Bonventre, 2015; Humphreys, 2018; Gewin, 2018**). We hypothesized that the accumulation of damage-associated PT cells, which show proinflammatory transcriptional signature (**Figure 1—figure supplement 5B,D and E**), creates an uncontrolled inflammatory milieu by interacting with resident and infiltrating myeloid cells such as macrophages and monocytes (**Ide et al., 2020**). To determine the intercellular interactions between damage-associated PT cells and myeloid cells, we used NicheNet, a computational algorithm tool that infers ligand-receptor interactions and downstream target genes (**Figure 4**, A-D), (**Browaeys et al., 2020**). We applied NicheNet to predict ligand-receptor pairs in which ligands from damage-associated PT cells interact with receptors in monocyte or macrophages (**Figure 4**, A and C), (**Browaeys et al., 2020**). Among the top five predicted ligands expressed in damage-associated PT cells, we

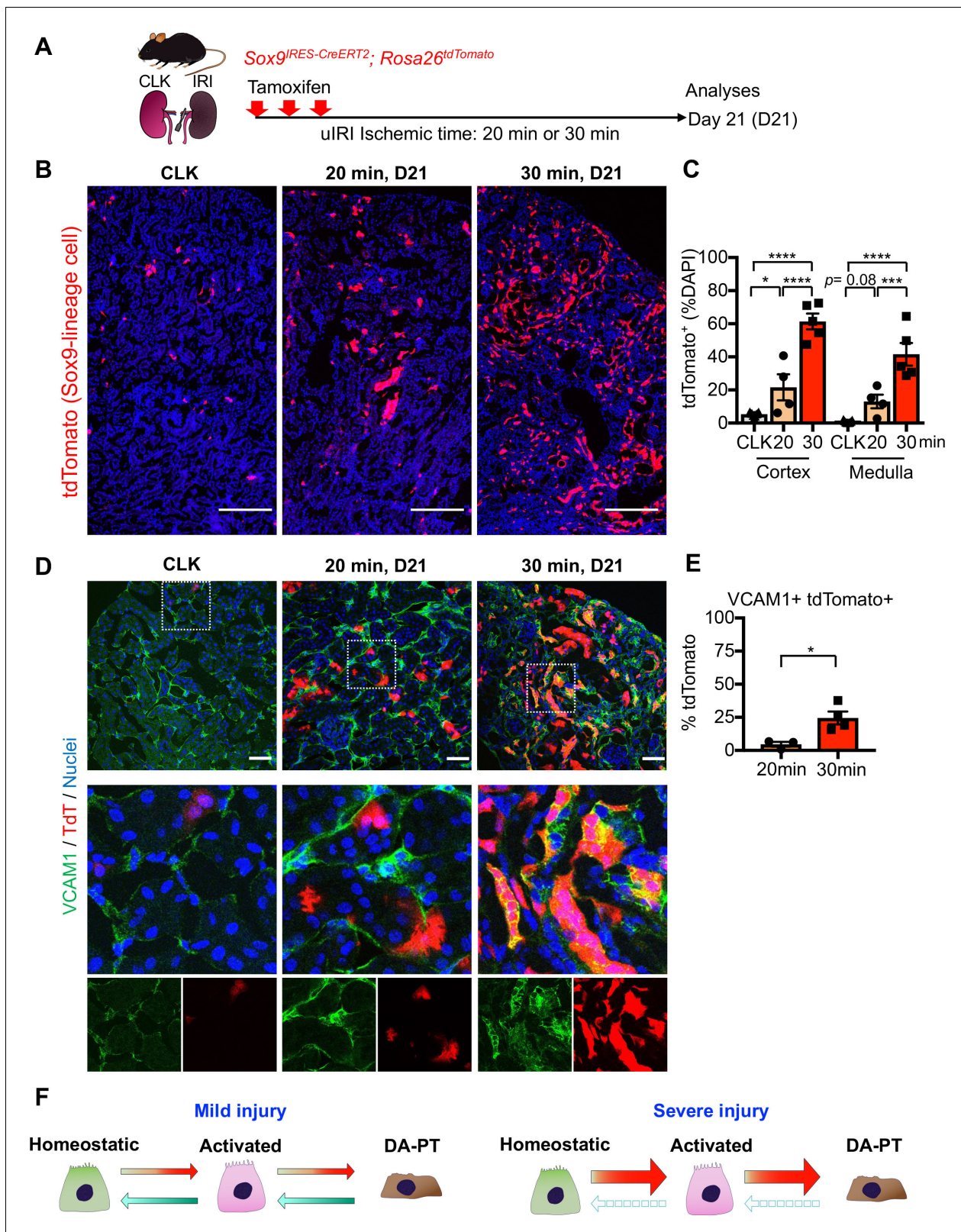


**Figure 3.** Lineage-tracing identifies the cellular plasticity of damage-associated PT cells. (A) Schematic of fate-mapping strategy using *Sox9<sup>IRES-CreERT2</sup>; Rosa26<sup>tdTomato</sup>* mice. Tamoxifen was administered three times on alternate days. Contralateral kidneys (CLK) were used as controls. (B) Distribution of tdTomato-expressing cells (Sox9-lineage cells) in contralateral (CLK), mild (20 min) and severe (30 min) IRI kidneys on day 21 (D21). (C) Quantification of tdTomato<sup>+</sup> area relative to DAPI<sup>+</sup> area in (B). DAPI was used for nuclear staining. N = 4-5. (D) Immunostaining for VCAM1 in Sox9-lineage-tagged cells. (E) Quantification of VCAM1<sup>+</sup> tdTomato<sup>+</sup> cells. (F) Schematic of cellular plasticity of damage-associated PT cells under mild and severe injury. Figure 3 continued on next page



Figure 3 continued

kidneys (post-IRI, day 21). Sox9-lineage cells express native tdTomato red fluorescence (TdT). Insets: individual fluorescence channels. (E) Quantification of double-positive cells in total tdTomato<sup>+</sup> cells in (D). N = 3–4. Note that more Sox9-lineage cells express VCAM1 after severe IRI (30 min) compared to mild IRI (20 min) on day 21. One-way ANOVA with post hoc multiple comparisons test and unpaired Student's t-test were used for (C) and (E), respectively. Scale bars, 200 μm in (B); and 50 μm in (D). \*p < 0.05; \*\*p < 0.01; \*\*\*p < 0.001; \*\*\*\*p < 0.0001. (F) Schematic illustration of PT cell state dynamics. Differentiated/mature PT cells are activated, transit into a molecularly distinct PT cell state (damage-associated PT cells in DA-PT cluster), and redifferentiate into their original state after mild injury (left). Severe injury prevents the redifferentiation of damage-associated PT cells into normal PT cell state, leading to the accumulation and persistence of damage-associated PT cells (right).

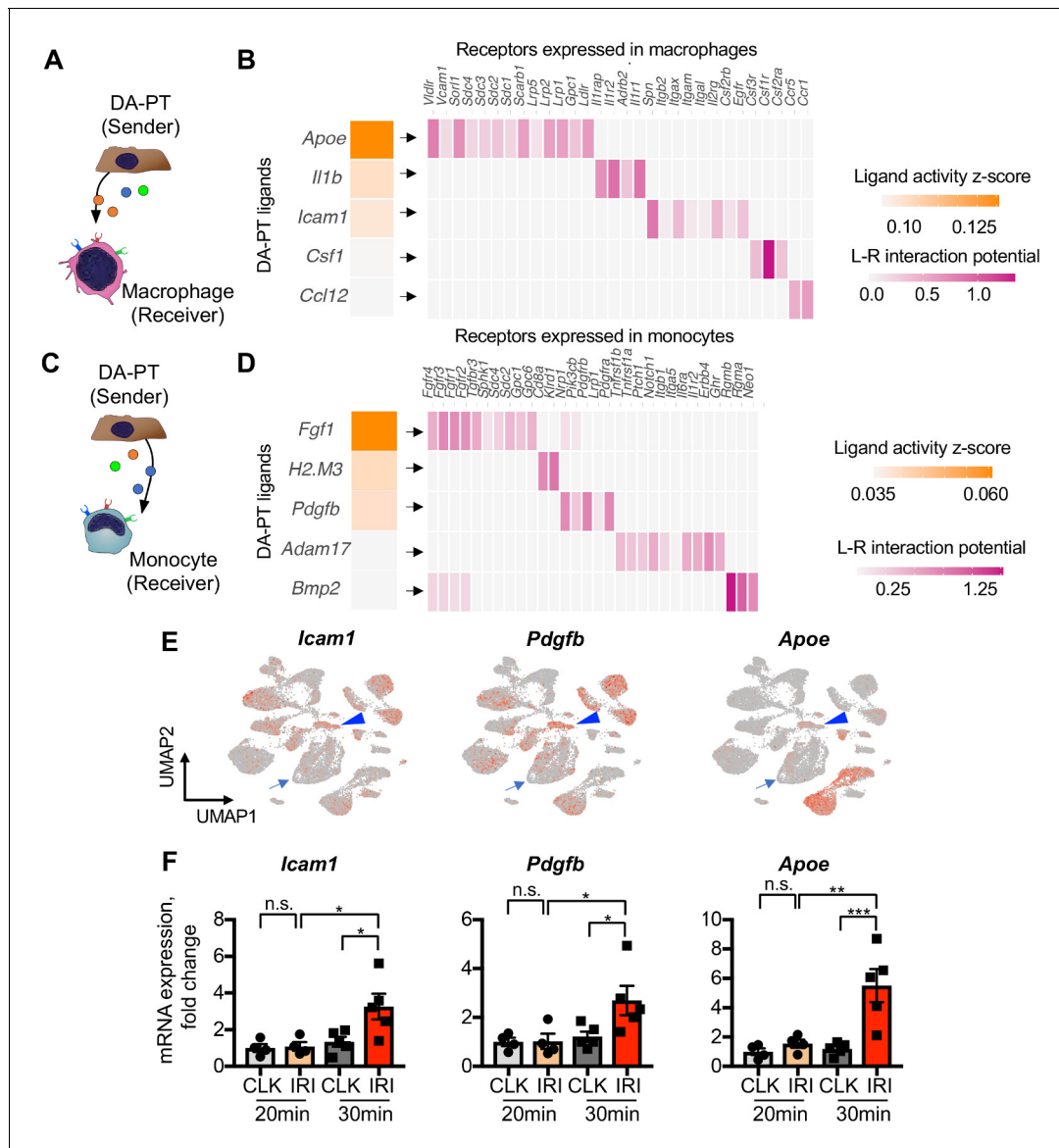


**Figure 4.** Damage-associated PT cells create a proinflammatory milieu with myeloid cells. (A) Schematic model of intercellular communications between damage-associated PT cells and macrophages. NicheNet was used to predict intercellular interactions using our integrated single-cell map of failed renal repair. (B) Predicted ligands from damage-associated PT cells and receptors in macrophages. (C) Schematic model of intercellular communications between damage-associated PT cells and monocytes. (D) Predicted ligands from damage-associated PT cells and receptors in monocytes. (E) UMAP plots showing the expression of indicated genes. Our integrated single-cell map of mouse failed renal repair is shown (See **Figure 1, B and C**). Arrowheads indicate damage-associated PT cells (DA-PT cluster). Arrows indicate differentiated PT cells (PT cluster). (F) Real-time PCR analyses of indicated gene expression. Post-IRI kidneys on day 21 that underwent mild (20 min) or severe (30 min) ischemia were used. N = 4–5. \*p < 0.05; \*\*p < 0.01; \*\*\*p < 0.001, one-way ANOVA with post hoc multiple comparisons test.

confirmed the enrichment of *Icam1*, *Pdgfb*, and *Apoe* expression in this cell state (**Figure 4E**, arrowheads). *Icam1* and *Pdgfb* have been implicated in human AKI (**Famulski et al., 2012**), and *Apoe* genetic variation has been linked with CKD progression (**Hsu et al., 2005**). As inferred by NicheNet, mRNA expression of *Icam1*, *Pdgfb*, and *Apoe* were markedly increased in the kidneys showing the accumulation of damage-associated PT cells compared to post-IRI kidneys without the accumulation (**Figure 4F**; 30 min vs. 20 min ischemia). These data delineate a complex inflammatory circuit within the damaged kidneys involving intercellular communication between damage-associated PT cells and myeloid cells that contribute to maladaptive renal repair.

## Damage-associated PT cells exhibit high ferroptotic stress after severe IRI

Next, we investigated the molecular mechanisms that are critical for cells to traverse between differentiated PT cells and damage-associated PT cells. To this end, we analyzed the transcriptional signature of PT cells in the differentiated/mature cluster to identify critical pathways to maintain this cellular state. We found that genes associated with glutathione metabolic processes and anti-oxidative stress response pathways are overrepresented in the differentiated mouse PT cell cluster (**Figure 5A**; **Figure 1—figure supplement 5F** and **Figure 5—figure supplement 1**). We also found that these pathways are enriched in normal differentiated human PT cells (**Figure 5A** and **Figure 5—figure supplement 2, A and B**; GSE131882). Mirroring these findings, oxidative stress-induced signaling pathways related to failed renal repair, such as cellular senescence and DNA damage responses (**Kishi et al., 2019**; **Canaud et al., 2019**), were highly enriched in damage-associated PT cells (**Figure 5—figure supplement 1**). Taken together, we propose that glutathione-mediated anti-oxidative stress responses are critical for maintaining the cellular identity of fully differentiated PT cells, and dysregulation of these pathways underlies the failure of damage-associated PT cells to redifferentiate into normal PT cell state.

Among the cellular stress pathways related to dysregulation of glutathione metabolism, ferroptotic stress and ferroptosis have been implicated in failed repair of human AKI and pathogenesis in mouse models of AKI, (**Figure 5B**), (**Stockwell et al., 2017**; **Dixon et al., 2012**; **Yang et al., 2014**; **Linkermann et al., 2014**; **Wenzel et al., 2017**; **Müller et al., 2017**). To investigate whether ferroptotic stress underlies the emergence and accumulation of damage-associated PT cells in addition to its known role in inducing cell death during maladaptive repair, we first tested the expression of the canonical anti-ferroptosis defense pathway, glutathione/GPX4 axis (**Figure 5B**). In agreement with the underrepresentation of glutathione metabolic process in damage-associated PT cells, the genes encoding the glutathione/GPX4 defense pathway were markedly downregulated in this PT cell state (DA-PT) compared to differentiated PT cells (PT), suggesting that damage-associated PT cells are potentially vulnerable to ferroptotic stress (**Figure 5C**).

We then analyzed the expression of ferroptotic stress biomarkers such as malondialdehyde (MDA, a lipid peroxidation product) and acyl-CoA synthetase long-chain family member 4 (ACSL4), which also regulate cellular sensitivity to ferroptosis (**Kagan et al., 2017**; **Doll et al., 2017**; **Müller et al., 2017**; **Kenny et al., 2019**; **Yuan et al., 2016**; **Li et al., 2019**). A recent pharmacological inhibitor study showed that ACSL4 is a reliable marker for ferroptotic stress in murine model of ischemic AKI (**Zhao et al., 2020**). We identified significant upregulation of *Acs14* in damage-associated PT cells in dot-plots (**Figure 5C**). The co-expression of markers for damage-associated PT cells and ferroptotic stress was confirmed by immunofluorescence for SOX9, MDA, and ACSL4 (**Figure 5, D-G**). We found that severe ischemia (30 min) induces more expression of ferroptotic stress markers in SOX9<sup>+</sup> cells than mild ischemic injury (20 min) (**Figure 5, E and G**). These data demonstrate that SOX9<sup>+</sup> damage-associated PT cells undergo high ferroptotic stress after severe ischemic injury.

To address whether the emergence of damage-associated PT cells is specific to IRI injury or appears in other cases of acute kidney injury, we investigated the co-expression of SOX9 and VCAM1 in models of toxic renal injury (aristolochic acid nephropathy, AAN) and obstructive renal injury (unilateral ureteral obstruction, UUO), which lead to severe fibrosis. By immunofluorescence analyses of SOX9 and VCAM1 co-expression, we found the emergence of damage-associated PT cells in both models (**Figure 6, A and C**). Furthermore, the SOX9-positive tubular epithelial cells in these models showed co-expression of ACSL4, suggesting that ferroptotic stress of damage-associated PT cells is a conserved response to kidney injury across various etiologies (**Figure 6, B and C**).

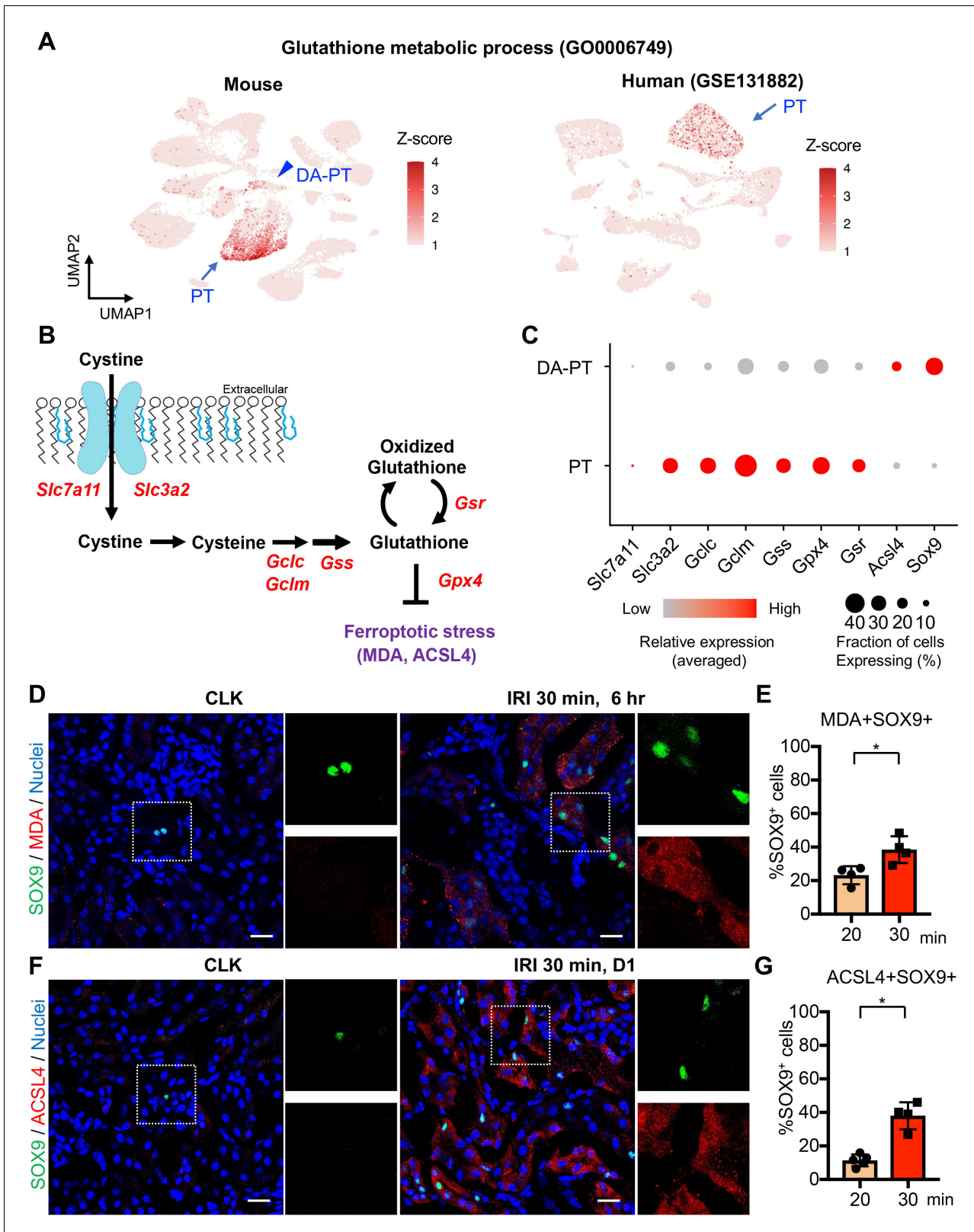


**Figure 5.** Damage-associated PT cells undergo high ferroptotic stress after severe IRI. (A) UMAP rendering of glutathione metabolic process in mouse and human kidneys. (B) A scheme showing glutathione-glutathione peroxidase 4 (GPX4) anti-ferroptotic defense pathway. *Slc7a11* and *Slc3a2* (system  $x_c^-$ ); *Gclc* and *Gclm* (glutamate-cysteine ligase); *Gss* (glutathione synthetase); *Gsr* (glutathione reductase); and *Gpx4*. MDA (malondialdehyde, a lipid peroxidation product) and ACSL4 (acyl-CoA synthetase long-chain family member 4) are markers for ferroptotic stress. (C) Dot plots show the relative expression and fraction of cells expressing various genes in DA-PT and PT cells. (D) Immunofluorescence images show SOX9 (green) and MDA (red) in CLK and IRI 30 min, 6 hr. (E) Bar graph shows the percentage of SOX9+ cells in MDA+SOX9+ cells at 20 and 30 min. (F) Immunofluorescence images show SOX9 (green) and ACSL4 (red) in CLK and IRI 30 min, D1. (G) Bar graph shows the percentage of SOX9+ cells in ACSL4+SOX9+ cells at 20 and 30 min. Figure 5 continued on next page

Figure 5 continued

expression of genes for glutathione-GPX4 axis, *Sox9*, and *Acs14*. (D) Immunostaining for SOX9 and MDA (6 hr post-IRI), and (E) quantification of double-positive cells in total SOX9<sup>+</sup> cells. N = 4. (F) Immunostaining for SOX9 and ACSL4 (1 day post-IRI), and (G) quantification of double-positive cells in total SOX9<sup>+</sup> cells. N = 4. Insets: individual fluorescence channels of the dotted box area. Note that severe ischemia (30 min) induces more ferroptotic stress markers (MDA and ACSL4) in SOX9<sup>+</sup> cells in damaged kidneys than mild ischemia (20 min). Wild-type C57BL/6J mice were used for (D) to (G). Scale bars, 20 μm in (D) and (F). \*p < 0.05. unpaired Student's t-test.

The online version of this article includes the following figure supplement(s) for figure 5:

**Figure supplement 1.** Gene ontology analyses identify enrichment of anti-oxidative stress defense genes in differentiated/mature PT cells.

**Figure supplement 2.** Characterization of human normal kidney single-nucleus RNA-seq data.

We then investigated whether molecularly similar damage-associated PT cells can be observed in human AKI. We analyzed scRNA-seq data from biopsy samples of two transplanted human kidneys with evidence of AKI and acute tubular injury but no evidence of rejection (GSE145927; **Figure 6D** and **Figure 6—figure supplement 1A**), (Malone et al., 2020). We found a cell population that is enriched for genes expressed in mouse damage-associated PT cells, including *SOX9*, *VCAM1*, *CDH6*, and *VIM*. This cellular population also showed decreased expression of homeostatic PT genes (*ALDOB*, *MIOX*, and *GPX4*) (**Figure 6**, State 3; D, and E). Trajectory inference using Monocle 3 suggests that damage-associated PT cells emerge from mature differentiated PT cells with high expression of homeostatic genes in human kidneys (PT to DA-PT-like in **Figure 6F**). Interestingly, the glutathione metabolic gene signature is high in mature PT cells and decreases along the trajectory to DA-PT-like cells (**Figure 6—figure supplement 1C**). These data suggest that the emergence of damage-associated PT cells is a mechanism of acute kidney injury and repair that is shared by humans and mice.

## Genetic induction of ferroptotic stress results in accumulation of inflammatory PT cells after mild injury

Our data suggest that severe injury, which induces more oxidative and ferroptotic stress than mild injury, causes the accumulation of inflammatory damage-associated PT cells and worsens long-term renal outcomes. We hypothesized that ferroptotic stress plays a crucial role in driving the accumulation of inflammatory PT cells and promoting maladaptive repair in addition to triggering cell death (ferroptosis). To test this hypothesis, we generated a mouse model that selectively and conditionally deletes *Gpx4* in *Sox9*-lineage cells (*Sox9*<sup>RES-CreERT2</sup>; *Gpx4*<sup>flox/flox</sup>, hereafter conditional knockout [cKO]; **Figure 7A**). Genetic deletion of *Gpx4* robustly induces ferroptotic stress and triggers ferroptosis (Yang et al., 2014; Friedmann Angeli et al., 2014). In this mouse line, exons 4–7 of the *Gpx4* allele, which include the catalytically active selenocysteine site of the GPX4 protein, is deleted in a tamoxifen-inducible manner selectively in *Sox9*-lineage cells. We subjected the cKO mice and littermate control mice to mild renal ischemic stress (ischemic time 22 min). This condition induces robust *Sox9-CreERT2* expression but does not induce the failed renal repair phenotype in control mice (*Gpx4*<sup>flox/flox</sup>). We induced *Gpx4* deletion at the time of injury by tamoxifen injection (**Figure 7A**). The littermate control mice were subjected to the same renal ischemic stress and tamoxifen. We confirmed successful deletion of GPX4 protein by immunofluorescence (**Figure 7—figure supplement 1, B and C**) and found that expression of the ferroptotic stress marker ACSL4 was increased on day 21 post-IRI in cKO kidneys compared to littermate kidneys that underwent the same ischemic stress (**Figure 7—figure supplement 1, D and E**). Contralateral uninjured kidneys from cKO mice only showed a minimum deletion of GPX4 as the *Sox9-CreERT2* activity is not induced in non-injured proximal tubular cells (See **Figure 3B** for CLK), (Kumar et al., 2015).

The post-ischemic cKO kidneys were atrophic and showed severe tubular injury on histological evaluation on day 21 and exhibited marked accumulation of KIM1<sup>+</sup>KRT8<sup>+</sup> injured tubular cells (**Figure 7**, B-D and **Figure 7—figure supplement 2**). By contrast, control littermate kidneys that underwent the same ischemic stress exhibited resolution of histological changes and fewer KIM1<sup>+</sup>KRT8<sup>+</sup> cells (**Figure 7**, C and D, and **Figure 7—figure supplement 2**). Contralateral kidneys from both genotypes showed neither increased KIM1 nor KRT8 expression (**Figure 7—figure supplement 3, A and C**). The post-ischemic cKO kidneys also exhibited massive accumulation of F4/80<sup>+</sup> macrophages, αSMA<sup>+</sup> myofibroblasts, and increased collagen synthesis (**Figure 7**, E-F; **Figure 7—figure**

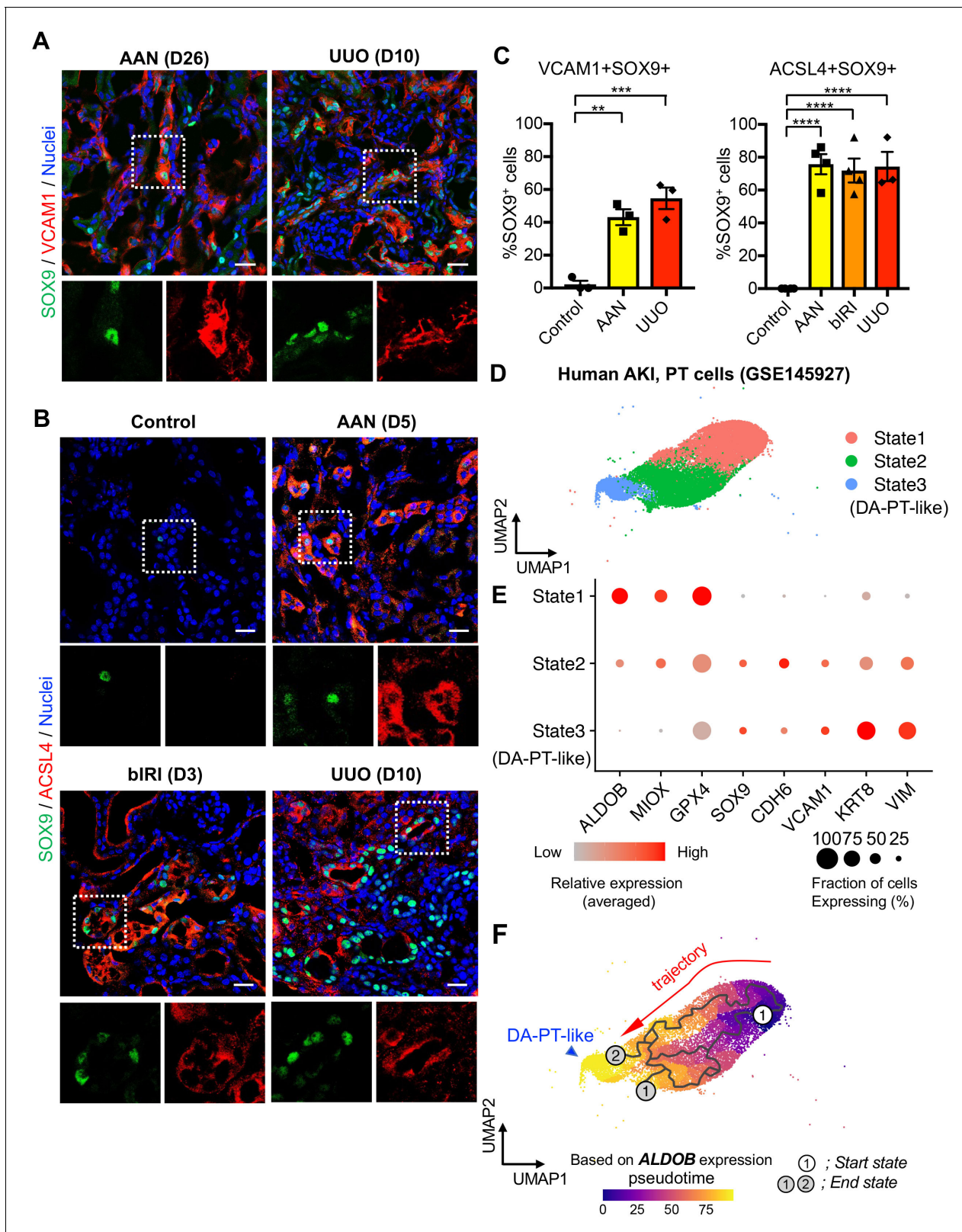


**Figure 6.** Damage-associated PT cells emerge after injury in mouse and human kidneys. (A) Immunostaining for SOX9 and VCAM1. Aristolochic acid nephropathy (AAN) and unilateral ureteral obstruction (UUO) models were used. Kidneys from wild-type C57BL/6J mice were harvested on day 26 (D26) for AAN and day 10 (D10) for UUO. Insets: individual fluorescence channels of the dotted box area. (B) Immunostaining for SOX9 and ACSL4. bIRI, bilateral IRI model. Kidneys were harvested on day 3 (D3) for bIRI, day 5 (D5) for AAN, and day 10 (D10) for UUO. Insets: individual fluorescence

Figure 6 continued on next page

Figure 6 continued

channels of the dotted box area. (C) Quantification of double-positive cells in total SOX9<sup>+</sup> cells from panel (A) and (B). Scale bars, 20  $\mu$ m. N = 3–4. \*\*p < 0.01; \*\*\*p < 0.001; \*\*\*\*p < 0.0001, one-way ANOVA with post hoc multiple comparisons test. (D) UMAP of the human proximal tubular cells from AKI kidneys. (E) Dot plots showing the expression of indicated genes. Note that PT cells in state 3 (DA-PT-like) show increased gene expressions of markers for mouse damage-associated PT cells (SOX9, VCAM1, CDH6) and reduced expression of homeostatic genes (ALDOB, MIOX, and GPX4). (F) Pseudotime trajectory analysis of PT clusters (PT and DA-PT-like cells). A region occupied with ALDOB<sup>high</sup> cells were set as a starting state. Arrow, predicted trajectory from PT cells to DA-PT-like cells.

The online version of this article includes the following figure supplement(s) for figure 6:

**Figure supplement 1.** Characterization of human AKI kidney single-cell RNA-seq data.

**supplement 3, B and C).** Then, we assessed the number of cell death by terminal deoxynucleotidyl transferase-mediated dUTP nick end labeling (TUNEL) assay, which detects ferroptotic cell death in *Gpx4*-deleted tissues (Friedmann Angeli et al., 2014). Consistent with the known role of GPX4 to prevent ferroptosis, genetic deletion of *Gpx4* led to the increased TUNEL<sup>+</sup> tubular epithelial cells in cKO kidneys (Figure 7, G and H; See Figure 7—figure supplement 4 for CLK). Collectively, these data indicate that genetic induction of ferroptotic stress in *Sox9*-lineage cells is sufficient to prevent normal renal repair after mild ischemic injury and to mimic the failed renal repair phenotype observed after severe ischemic injury.

We then investigated if the number of damage-associated PT cells was increased in the *Gpx4* cKO kidneys after mild ischemic injury. While VCAM1 is strongly induced in damage-associated PT cells and serves as a reliable marker, it is also expressed weakly in F4/80<sup>+</sup> macrophages and endothelin (EMCN)<sup>+</sup> endothelial cells after kidney injury (Figure 1—figure supplement 6A; see UMAP). For the precise quantification of damage-associated PT cells, we co-stained the kidneys with VCAM1, EMCN, and F4/80, and scored VCAM1<sup>+</sup>F4/80<sup>-</sup>EMCN<sup>-</sup> cells as damage-associated PT cells (Figure 8, B and C; and Figure 7—figure supplement 3D). Supporting our hypothesis, we observed increased numbers of VCAM1<sup>+</sup>EMCN<sup>-</sup>F4/80<sup>-</sup> cells in post-ischemic cKO kidneys on day 21, while the value was at a baseline level in control littermate kidneys that underwent the same mild ischemic stress (Figure 8, B and C). We further employed a genetic fate-mapping strategy in *Gpx4*-deficient *Sox9*-lineage cells by generating a mouse line that harbors *Sox9*<sup>RES-CreERT2</sup>; *Gpx4*<sup>flox/flox</sup>; *Rosa26*<sup>tdTomato</sup> alleles. Confocal imaging identified the colocalization of tdTomato (*Sox9*-lineage) and VCAM1 and ACSL4 in the post-IRI cKO kidneys (Figure 8D). Other molecular markers of damage-associated PT cell state, such as *Cdh6* and *Sox9*, were also increased in cKO kidneys on day 21 post-IRI (Figure 8E). These VCAM1<sup>+</sup> cells were also positive for SOX9 (Figure 8F). In situ hybridization confirmed robust *Cdh6* expression in tubular epithelial cells in post-ischemic cKO kidneys (Figure 8G and Figure 7—figure supplement 3E). These data substantiate our model that ferroptotic stress drives the accumulation of damage-associated PT cells by preventing redifferentiation of these transient inflammatory epithelial cells into normal PT cell state and augments renal inflammation and fibrosis (Figure 8H).

### Pharmacological inhibition of ferroptotic stress prevents the accumulation of inflammatory PT cells and ferroptosis after ischemia-reperfusion injury

We next investigated whether pharmacological inhibition of ferroptosis blunts the dynamic changes seen in proximal tubular cells. We administered liproxstatin-1, an in vivo active ferroptosis inhibitor that scavenges lipid peroxides (Friedmann Angeli et al., 2014), to our cKO mice that underwent mild renal ischemia (Figure 9A). The same volume of vehicle solution (1% dimethyl sulfoxide in phosphate-buffered saline) was administered to cKO and littermate controls (*Gpx4*<sup>flox/flox</sup>), and these animals underwent the same procedure of unilateral IRI. While vehicle-treated IRI-kidneys of control genotype did not show renal atrophy, cKO IRI-kidneys with daily vehicle injections exhibited renal atrophy (Figure 9B). We further confirmed effective genetic targeting in our cKO IRI-kidneys from the vehicle and liproxstatin-1-treated groups by using tdTomato-lineage tracing and GPX4 immunohistochemistry (Figure 9—figure supplement 1, B and C). Daily administration of liproxstatin-1 potently mitigated the renal atrophy and reduced expression of renal tubular injury markers in cKO IRI-kidneys (KIM1 and KRT8; Figure 9, B-D; Figure 9—figure supplement 2). Notably, liproxstatin-1

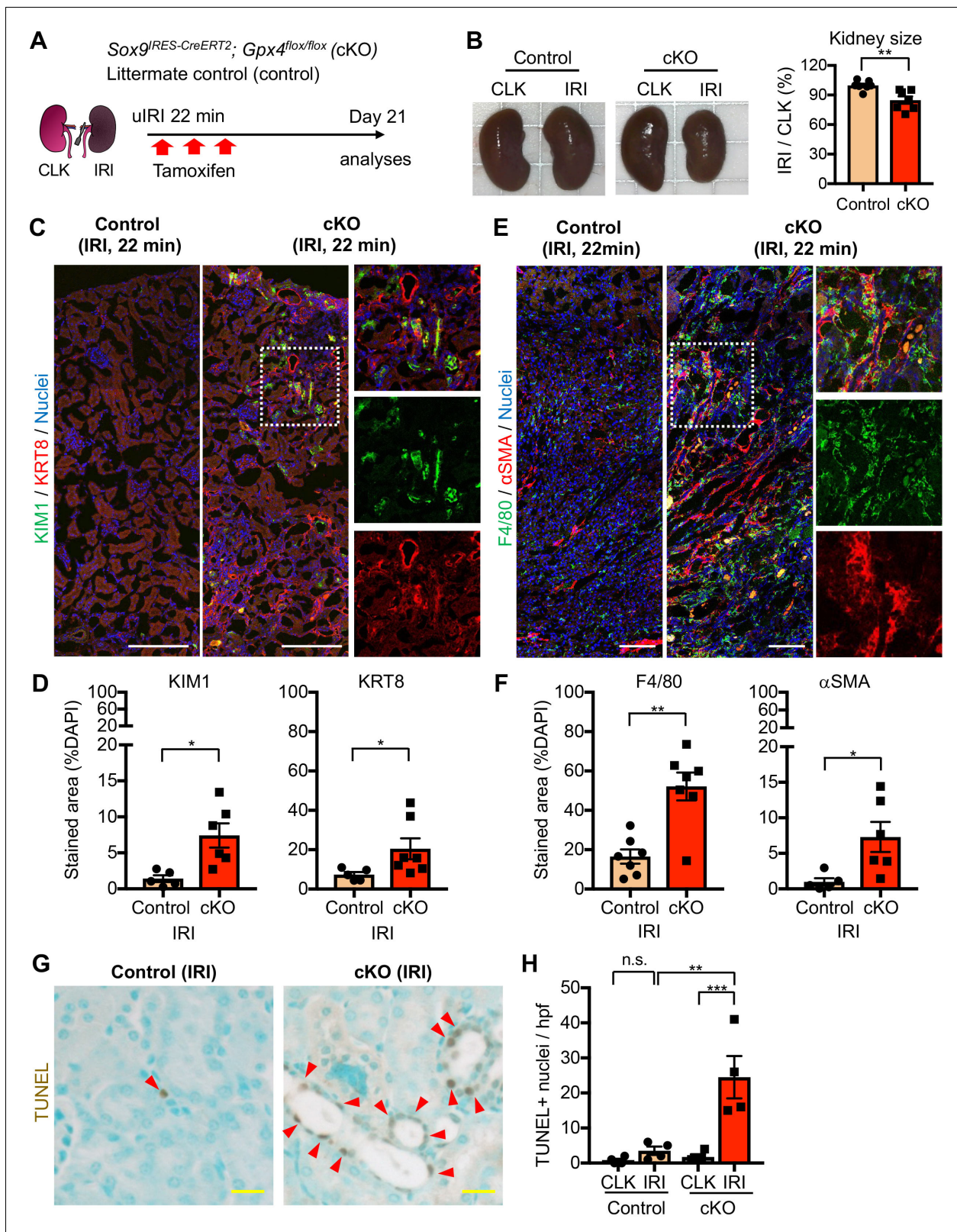


**Figure 7.** Genetic induction of ferroptotic stress to Sox9-lineage cells augments kidney injury. (A) Experimental workflow for *Gpx4* deletion in Sox9-lineage cells. uIRI, unilateral IRI (ischemic time 22 min). Kidneys were harvested on day 21 post-IRI. cKO mice and their littermate controls were subjected to the same ischemic stress and tamoxifen treatment. *Gpx4* is deleted in Sox9-lineage cells after IRI with tamoxifen administration. (B) The deletion of *Gpx4* results in renal atrophy. Relative size of post-IRI kidneys compared to contralateral kidneys (CLK) was quantified. Control, littermate control. Figure 7 continued on next page

Figure 7 continued

control. N = 7. (C) and (D) Immunostaining for tubular injury markers (KIM1 and KRT8). IRI kidneys from cKO and control littermates are shown. CLK did not show KIM1 or KRT8 staining. Quantification of KIM1 or KRT8-positive area over the DAPI<sup>+</sup> area is shown in (D). N = 5–7. (E) and (F) Immunostaining for F4/80 and  $\alpha$ SMA. IRI kidneys from cKO and control littermates are shown. Quantification of F4/80 or  $\alpha$ SMA-positive area over the DAPI<sup>+</sup> area is shown in (F). N = 5–7. Insets: individual fluorescence channels of the dotted box area. (G) and (H) TUNEL staining for evaluating cell death.

Quantification of TUNEL-positive nuclei is shown in (H). N = 4. Arrowheads, TUNEL<sup>+</sup> nuclei. Abbrev: hpf, high power field. Unpaired t-test for (D) and (F). One-way ANOVA with post hoc multiple comparison test for (H). Scale bars, 100  $\mu$ m in (C) and (E); 20  $\mu$ m in (G).

The online version of this article includes the following figure supplement(s) for figure 7:

**Figure supplement 1.** Genetic deletion of *Gpx4* leads to augmented ferroptotic stress after mild IRI.

**Figure supplement 2.** Genetic deletion of *Gpx4* leads to severe kidney injury after mild IRI.

**Figure supplement 3.** Genetic deletion of *Gpx4* leads to the accumulation of damage-associated PT cells.

**Figure supplement 4.** Genetic deletion of *Gpx4* leads to cell death of tubular epithelial cells.

prevented the accumulation of SOX9+VCAM1+ proximal tubular cells (Figure 9, E and F). Quantitative RT-PCR analyses confirmed that the expression of *Sox9*, *Vcam1*, and *Cdh6* (DA-PT markers) were all reduced by liproxstatin-1 to the same level as in contralateral uninjured kidneys (Figure 9G). Moreover, TUNEL staining showed a significant reduction of TUNEL+ cells in the liproxstatin-1-treated IRI-cKO kidneys compared to the vehicle-treated IRI-cKO kidneys (Figure 9, H and I). Collectively, liproxstatin-1 potentially ameliorated the pathologic changes of proximal tubular cells and overall damage of *Gpx4*-deficient kidneys that underwent IRI (Figure 9J).

## Discussion

By using complementary scRNA-seq and mouse genetic approaches in several experimental models of renal injury and repair, our study revealed novel mechanisms regulating proximal tubular cell states that underlie renal repair and regeneration. By detailed characterization of damage-associated PT cells in our single-cell map of failed repair, we identified that this PT state significantly downregulates the canonical anti-ferroptosis defense pathway, making them potentially vulnerable to ferroptotic stress. Genetic induction of ferroptotic stress after mild injury was sufficient to prevent the redifferentiation of damage-associated PT cells into the normal PT cell state, leading to the accumulation and persistence of inflammatory PT cells that promote maladaptive repair. Our data collectively advances our understanding of the ferroptotic cell death pathway by identifying a novel role of ferroptotic stress in promoting and accumulating pathologic cellular state beyond its known role to trigger non-apoptotic regulated cell death (ferroptosis). GPX4 is a key coordinator of proximal tubular cell fate for renal repair and regeneration by preventing both cell death and cell death-independent pathologic changes after IRI.

Unbiased clustering of cells clearly separates damage-associated PT cells from homeostatic and activated differentiated PT cells, indicating that damage-associated PT cells represent a unique cellular status. We also found a molecularly similar PT cell state in kidneys of patients with acute kidney injury. Similar to our current findings, we and others have identified the emergence of molecularly distinct epithelial cells during the process of lung injury and repair (Kobayashi et al., 2020; Choi et al., 2020; Strunz et al., 2020). These novel transient cells are termed as pre-alveolar type-1 transitional cell state (PATS), alveolar differentiation intermediate, and damage-associated transient progenitors. They originate from alveolar type two epithelial cells and differentiate into type one alveolar epithelial cells (Kobayashi et al., 2020; Choi et al., 2020; Strunz et al., 2020). PATS and PATS-like cells in humans accumulate during failed lung repair and fibrosis (Kobayashi et al., 2020), as in the case of maladaptive repair of kidneys. Molecular mechanisms underlying the accumulation of these transitional cell state include hypoxia, inflammation, and DNA damage. All these pathways promote maladaptive renal repair by altering PT cell states (Strausser et al., 2018; Liu et al., 2017; Ferenbach and Bonventre, 2015; Kishi et al., 2019). These data suggest that the emergence of molecularly distinct epithelial cell states and their persistence/accumulation is a general mechanism of maladaptive repair in multiple organs across mice and humans.

The complexity of proximal tubular cell states in renal injury and repair processes has been recently identified at single-cell resolution (Kirita et al., 2020; Rudman-Melnick et al., 2020). A recent study investigated PT cellular heterogeneity using single-nucleus RNA sequencing in a mouse



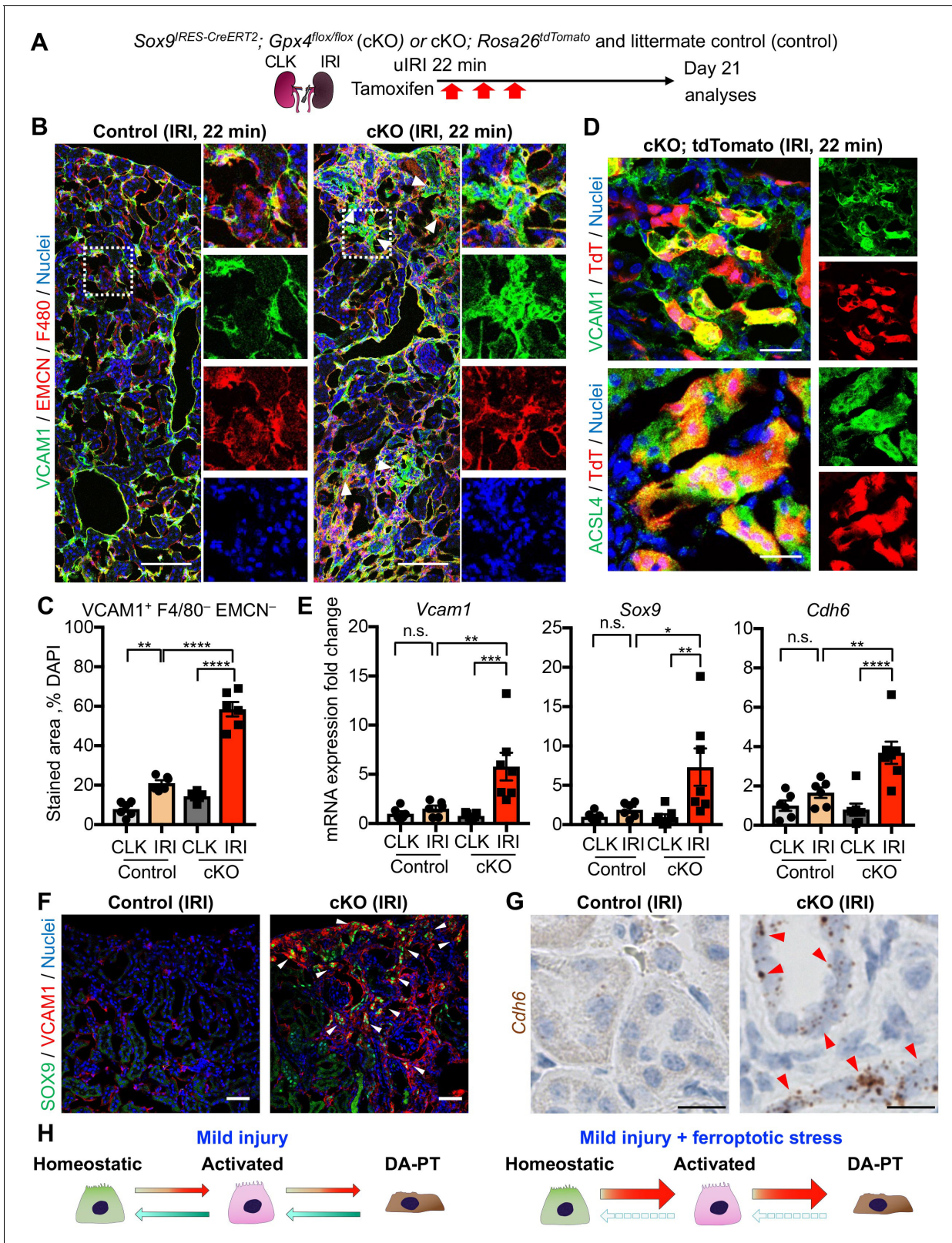


**Figure 8.** Genetic induction of ferroptotic stress induces the accumulation of damage-associated PT cells after mild injury. (A) Schematic representation of experimental workflow. tdTomato-lineage tracing was employed to detect Sox9-lineage cells. cKO mice and their littermate controls were subjected to the same ischemic stress (ischemic time, 22 min) and tamoxifen treatment. Kidneys were harvested on day 21 post-IRI. (B) and (C) Immunostaining for VCAM1, EMCN (endomucin), and F4/80. IRI kidneys from cKO and control littermates (control) are shown. Quantification of VCAM1<sup>+</sup>EMCN<sup>-</sup>F4/80<sup>-</sup> area  
 Figure 8 continued on next page

## Figure 8 continued

over the DAPI<sup>+</sup> area is shown in (C). N = 6. (D) Immunostaining for VCAM1, ACSL4, and native tdTomato (TdT) fluorescence. Insets: individual fluorescence channels. (E) Real-time PCR analyses of indicated gene expression. Whole kidney lysates were used. N = 6–7. \*p < 0.05; \*\*p < 0.01; \*\*\*p < 0.001; \*\*\*\*p < 0.0001, one-way ANOVA with post hoc multiple comparisons test for (C) and (E). (F) Immunostaining for SOX9 and VCAM1. Arrowheads indicate double-positive cells (damage-associated PT cells). (G) ISH for *Cdh6* expression. Red arrowheads indicate *Cdh6*-positive renal tubular cells. Scale bars, 100 μm in (B); 20 μm in (D); 50 μm in (F); and 10 μm in (G). (H) Schematic illustration of PT cell state dynamics. Differentiated/mature PT cells are activated, transit into a damage-associated inflammatory PT cell state (DA-PT), and redifferentiate to their original state after mild injury. Ferroptotic stress prevents the redifferentiation of damage-associated PT cells into normal PT cell state, leading to the accumulation of the pathologic PT cells that actively produce inflammatory signals.

model of bilateral renal IRI. The paper revealed multiple novel PT cellular states, ranging from severely injured cells, cells repairing from injury, and cells undergoing failed repair (Kiritā et al., 2020). Interestingly, the damage-associated PT cells reported here shares some of the transcriptional signatures with so-called failed repair proximal tubular cells (FR-PTC), such as *Vcam1*, *Cp*, *Akap12*, and *Dcdc2a* among the Top 20 transcriptional signature of FR-PTC. In contrast, we also found some differences between the damage-associated PT cells and FR-PTC. The most highly expressed genes in FR-PTC (ex. *Kcnip4*, *Dock10*, *Pdgfd*, *ErbB4*, and *Psd3*) were not expressed in damage-associated PT cells and vice versa. Moreover, damage-associated PT cells act like a transient cell state. They redifferentiate to the homeostatic PT cell state after mild injury while they accumulate after severe injury. Damage-associated PT cells may represent a broad transient cell state, including FR-PTC.

Another study profiled juvenile (4-week-old) mouse kidneys that underwent 30 min unilateral IRI (Rudman-Melnick et al., 2020). Unlike adult kidneys, the kidneys at this stage showed marked regenerative ability and showed successful repair. The study found transient induction of nephrogenic transcriptional signature (ex. *Sox4*, *Cd24a*, *Npnt*, *Lhx1*, *Osr2*, *Foxc1*, *Hes1*, *Pou3f3*, and *Sox9*) in damaged PT cells during the injury–repair process (Rudman-Melnick et al., 2020). While our transcriptional analyses of damage-associated PT cells indicate they are in a dedifferentiated state, they do not show a nephrogenic signature at the level of damaged juvenile kidneys (i.e. damage-associated PT cells were positive for *Sox4*, *Npnt*, and *Cd24a*, and *Sox9*, but negative for *Lhx1*, *Osr2*, *Foxc1*, *Hes1*, and *Pou3f3*). The differences in reactivation of developmental genes between adult and juvenile kidneys may underlie the age-dependent decline of reparative capacity of mouse and human kidneys. Future studies testing the proximal tubular heterogeneity and spatiotemporal dynamics in additional renal injury models in young and aged animals may offer further insights into molecular mechanisms governing proximal tubular cell plasticity and identify therapeutic targets.

It has been largely believed that ferroptotic stress reduces functional renal epithelial cells by intercellular propagation of ferroptotic cell death (synchronized cell death) and induces so-called necroinflammation (Linkermann et al., 2014; Friedmann Angeli et al., 2014; Li et al., 2019; Strunz et al., 2020). Consistent with this notion, we observed the accumulation of TUNEL<sup>+</sup> tubular epithelial cells in cKO kidneys. In addition to inducing ferroptosis in some tubular epithelial cells, to our surprise, our genetic knockout studies showed that excess ferroptotic stress in regenerating PT cells drives the accumulation, but not reduction, of damage-associated PT cells that augment renal inflammation. Specific gene-expression signatures indicate that damage-associated PT cells are not merely severely injured cells on the pathway to cell death but a unique functional cell state. The cells are enriched for expression of renal developmental genes such as *Sox4* and *Sox9*. SOX9 is a previously described transcription factor essential for renal repair (Kang et al., 2016; Kumar et al., 2015), and SOX4 regulates epithelial mesenchymal transition in different disease contexts (Tiwari et al., 2013). Moreover, damage-associated PT cells are actively involved in renal inflammation by interacting with myeloid cells through producing cytokines and chemokines. Thus, ferroptotic stress not only promotes the alteration of cell state but makes it irreversible, leading to the pathologic accumulation of cells that actively produce inflammatory and fibrogenic signals.

In summary, our study broadens the roles of ferroptotic stress from one that is restricted to the induction of regulated cell death (ferroptosis) to include the promotion and accumulation of a pathologic cell state, processes that underlie maladaptive repair. Understanding the molecular mechanisms by which ferroptotic stress controls these processes in vivo would open a new avenue for currently available and prospective anti-ferroptotic reagents to enhance tissue repair/regeneration in

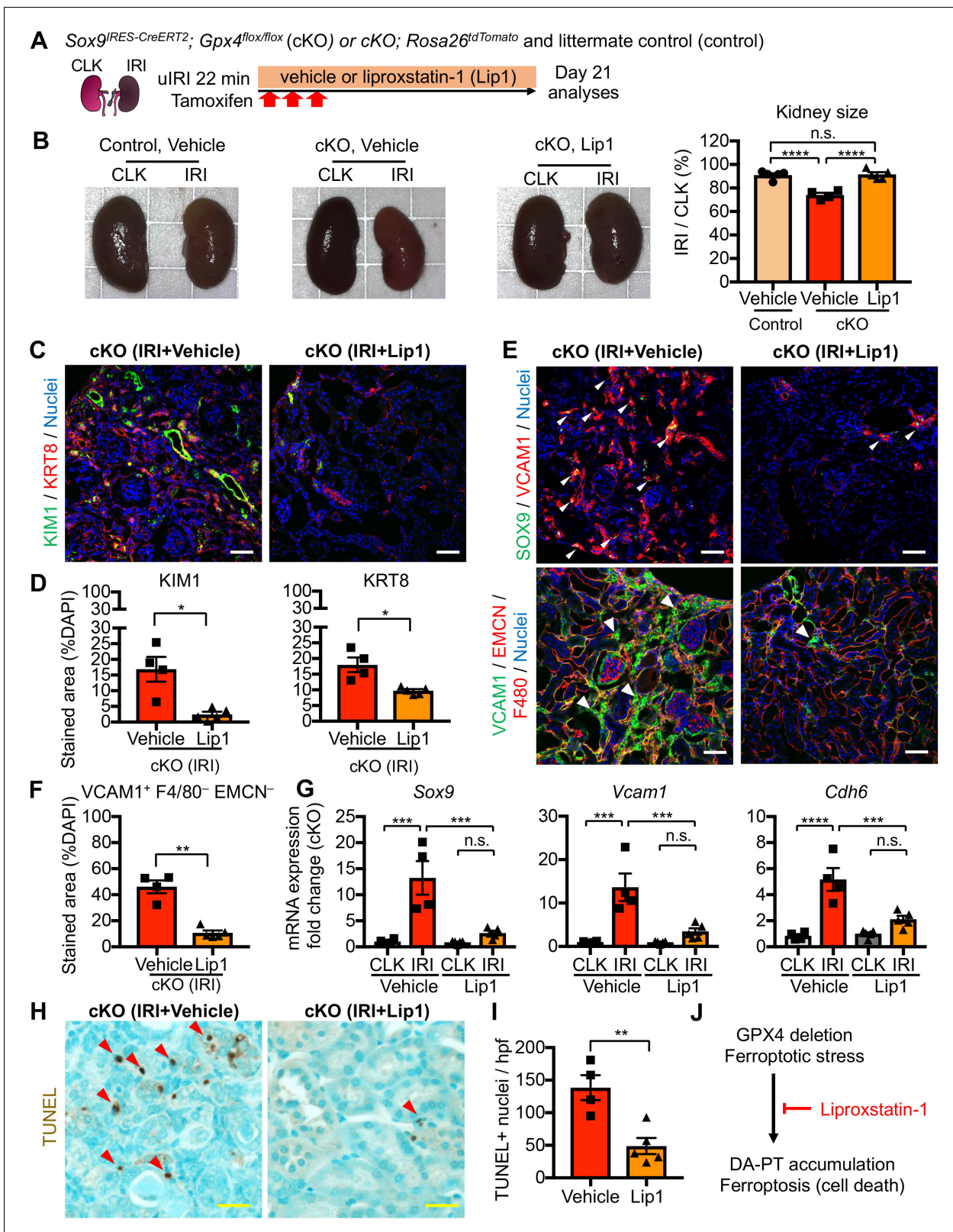


**Figure 9.** Pharmacological inhibition of ferroptotic stress blunts the accumulation of damage-associated PT cells and cell death. (A) Schematic representation of experimental workflow. All mice (cKO and control littermates) were subjected to the same ischemic stress (ischemic time, 22 min, unilateral IRI) and tamoxifen treatment. The same volume of vehicle was administered to the control groups (control vehicle and cKO vehicle). Kidneys were harvested on day 21 post-IRI. (B) Liproxstatin-1 prevents renal atrophy. Relative size of post-IRI kidneys compared to contralateral kidneys (CLK) Figure 9 continued on next page

Figure 9 continued

was quantified. Control, littermate control. N = 4–5. (C and D) Immunostaining for KIM1 and KRT8. IRI kidneys from cKO are shown. Quantification of immunostained area over the DAPI<sup>+</sup> area is shown in (D). N = 4–5. (E and F) Immunostaining for SOX9 and VCAM1. Quantification of VCAM1<sup>+</sup>EMCN<sup>+</sup>F4/80<sup>+</sup> area over the DAPI<sup>+</sup> area is shown in (F). Arrowheads indicate damage-associated PT cells. (G) Real-time PCR analyses of indicated gene expression. Whole kidney lysates were used. N = 4–5. (H) and (I) TUNEL staining for evaluating cell death. Quantification of TUNEL-positive nuclei is shown in (I). N = 4–5. Red arrowheads indicate TUNEL<sup>+</sup> tubular epithelial cells. Scale bars, 50 μm in (C) and (E); and 20 μm in (H). \*p < 0.05; \*\*p < 0.01; \*\*\*p < 0.001; \*\*\*\*p < 0.0001, unpaired t-test for (D), (F), and (I); One-way ANOVA with post hoc multiple comparisons test for (G). (J) Liproxstatin-1 improves renal repair after IRI.

The online version of this article includes the following figure supplement(s) for figure 9:

**Figure supplement 1.** Liproxstatin-1 potently reduced ferroptotic stress in the absence of GPX4.

**Figure supplement 2.** Liproxstatin-1 potently mitigated ferroptotic stress-induced pathologic changes in the absence of GPX4.

multiple organs. Our studies provide a scientific foundation for future mechanistic and translational studies to enhance renal repair and regeneration by modulating anti-ferroptotic stress pathways to prevent AKI to CKD transition in patients.

## Materials and methods

### Key resources table

Reagent type (species) or resource	Designation	Source or reference	Identifiers	Additional information
Genetic reagent ( <i>M. musculus</i> )	C57BL/6J	The Jackson laboratory	RRID:IMSR_JAX:020940	
Genetic reagent ( <i>M. musculus</i> )	Sox9 <sup>REScreERT2</sup>	The Jackson laboratory	RRID:MGI:4947114	
Genetic reagent ( <i>M. musculus</i> )	Rosa26 <sup>tdTomato</sup>	The Jackson laboratory	RRID:IMSR_JAX:007914	
Genetic reagent ( <i>M. musculus</i> )	Gpx4 <sup>fllox</sup>	The Jackson laboratory	RRID:IMSR_JAX: 027964	
Antibody	Anti-SOX9 (Rabbit monoclonal)	Abcam (ab196450)	RRID:AB_2665383	Clone EPR14335 IF: 1:200
Antibody	Anti-SOX9 (Rabbit monoclonal)	Abcam (ab185966)	RRID:AB_2728660	Clone EPR14335-78 IF: 1:200
Antibody	Anti-KIM1 (goat polyclonal)	R and D systems (AF1817)	RRID:AB_2116446	IF: 1:400
Antibody	Anti-NGAL (rat monoclonal)	Abcam (ab70287)	RRID:AB_2136473	IF: 1:400
Antibody	Anti-GPX4 (Rabbit monoclonal)	Abcam (ab125066)	RRID:AB_10973901	Clone EPNCIR144 IF: 1:200
Antibody	Anti-F4/80 (Rat monoclonal)	Bio-Rad (MCA497)	RRID:AB_2098196	Clone C1:A3-1 IF: 1:200
Antibody	Anti-Endomucin (Rat monoclonal)	Abcam (ab106100)	RRID:AB_10859306	Clone V.7C7.1 IF: 1:200
Antibody	Anti-KRT8 (Rat monoclonal)	DSHB (TROMA-1)	RRID:AB_531826	IF: 1:200
Antibody	Anti-αSMA (mouse monoclonal)	Sigma (C6198)	RRID:AB_476856	Clone 1A4 IF: 1:200
Reagent, commercial	LTL	Vector laboratories (B-1325 and FL-1321)	RRID:AB_2336558	IF: 1:200
Antibody	Anti-MDA (rabbit polyclonal)	Abcam (Ab6463)	RRID:AB_305484	IF: 1:200
Antibody	Anti-ACSL4 (rabbit monoclonal)	Abcam (Ab204380) (Ab155282)	RRID:AB_2714020	Clone: EPR8640 IF: 1:200

Continued on next page

Continued

Reagent type (species) or resource	Designation	Source or reference	Identifiers	Additional information
Antibody	Anti-VCAM1 (rabbit monoclonal)	CST 39036S 39301S	RRID:AB_2799146	Clone: D8U5V IF: 1:100
Commercial assay, kit	RNAScope probe-Mm-Cdh6	Advance Cell Diagnosis (Cat. 519541)		
Commercial assay, kit	RNAScope Intro Pack 2.5 HD Reagent Kit Brown Mm	Advance Cell Diagnosis (Cat. 322371)		
software, algorithm	ImageJ	NIH, Bethesda, MD (Version 1.52P)	RRID:SCR_003070	<a href="https://imagej.nih.gov/ij/">https://imagej.nih.gov/ij/</a>
Software, algorithm	GraphPad Prism		RRID:SCR_002798	<a href="https://www.graphpad.com/scientific-software/prism/">https://www.graphpad.com/scientific-software/prism/</a>
Software, algorithm	Seurat		RRID:SCR_016341	<b>Stuart et al., 2019</b> <a href="https://satijalab.org/seurat/get_started.html">https://satijalab.org/seurat/get_started.html</a>
Software, algorithm	Monocle 3		RRID:SCR_018685	<b>Cao et al., 2019</b> <a href="https://cole-trapnell-lab.github.io/monocle3/">https://cole-trapnell-lab.github.io/monocle3/</a>
Software, algorithm	Velocyto.R			<b>La Manno et al., 2018</b> <a href="https://github.com/velocyto-team/velocyto.R">https://github.com/velocyto-team/velocyto.R</a>
Software, algorithm	NicheNet			<b>Browaeys et al., 2020</b> <a href="https://github.com/saeyslab/nichenetr/blob/master/vignettes/seurat_wrapper.md">https://github.com/saeyslab/nichenetr/blob/master/vignettes/seurat_wrapper.md</a>
Software, algorithm	RStudio		RRID:SCR_000432	<a href="http://www.rstudio.com/">http://www.rstudio.com/</a>
Commercial reagent	Liberase	Roche (291963)		0.3 mg/ml
Commercial reagent	Hyaluronidase	Sigma (H4272)		10 µg/mL
Commercial reagent	Trypsin	Corning (45000–664)		0.25%
Chemical compound, drug	Tamoxifen	Sigma (T5648)		100 mg/kg
Chemical compound, drug	Liproxstatin-1	Selleckchem (S7699)		10 mg/kg
Chemical compound, drug	Aristolochic acid	Sigma (A9451)		6 mg/kg
Commercial assay, kit	TUNEL staining	Abcam (Ab206386)		

## Animals

All animal experiments were approved by the Institutional Animal Care and Use Committee at Duke University and performed according to the IACUC-approved protocol (A051-18-02 and A014-21-01) and adhered to the NIH Guide for the Care and Use of Laboratory Animals. The following mouse lines were used for our study; *Sox9<sup>lRES-CreERT2</sup>* (**Furuyama et al., 2011**), *Rosa26<sup>tdTomato</sup>* (Jackson lab, stock #007914), (**Madisen et al., 2010**), *Gpx4<sup>flox</sup>* (Jackson lab, stock# 027964), (**Yoo et al., 2012**), and C57BL/6J (Jackson lab, stock #000664). Mice were backcrossed into a C57BL/6J background at least three times and maintained in our specific-pathogen-free facility. Timed deletion of the *Gpx4* gene and fate-mapping was achieved using *Sox9<sup>lRES-CreERT2</sup>* knock-in mouse line with three doses of intraperitoneal injections of tamoxifen (100 mg/kg body weight, Sigma, St. Louis MO) on alternate days. The first dose of tamoxifen was administered immediately before the surgical intervention. All tested animals were included in data analyses, and outliers were not excluded. To avoid confounding

effects of age and strain background, littermate controls were used for all phenotype analyses of genetically modified mouse lines. Animals were allocated randomly into the experimental groups and analyses. The operators were blinded to mouse genotypes when inducing surgical injury models. To determine experimental sample sizes to observe significant differences reproducibly, data from our previous studies were used to estimate the required numbers. The number of biological replicates is represented by N in each figure legend. Experiments were performed on at least three biological replicates.

## Mouse models of renal injury and repair

Adult male mice aged between 8 and 16 weeks were used for all the models described below. The mice were euthanized, and kidneys were harvested for analyses. For the unilateral IRI (uIRI) model, ischemia was induced by the retroperitoneal approach on the left kidney for 20 min (mild IRI), 22 min (mild IRI in cKO studies), or 30 min (severe IRI) by an atraumatic vascular clip (Roboz, RS-5435, Gaithersburg, MD), as previously reported (*Nezu et al., 2017; Fu et al., 2018*). Mice were anesthetized with isoflurane and provided preemptive analgesics (buprenorphine SR). The body temperature of mice was monitored and maintained on a heat-controlled surgical pad. For the bilateral IRI (bIRI) model, ischemia was induced by the retroperitoneal approach on both kidneys for 22 min. The mice were received intraperitoneal injections of 500  $\mu$ l of normal saline at the end of surgery. For the unilateral ureteral obstruction (UUO) model, the left ureter was tied at the level of the lower pole of the kidney, and the kidneys were harvested on day 10. For the aristolochic acid nephropathy (AAN) model, we used acute and chronic models, as we previously described (*Ren et al., 2020*). For the acute AAN model, three doses of 6 mg/kg body weight aristolochic acid (Sigma, A9451) in phosphate-buffered saline (PBS) were administered daily intraperitoneally to the male mice. For the chronic AAN model, six doses of 6 mg/kg body weight aristolochic acid in phosphate-buffered saline (PBS) were administered on alternate days over 2 weeks intraperitoneally to the male mice. The same volume of PBS was injected to control animals (*Ren et al., 2020; Dickman et al., 2011*). Contralateral kidneys (CLK), sham-treated kidneys, and vehicle-injected kidneys were used as controls depending on the models used. The numbers and dates of treatment are indicated in the individual figure legends and experimental schemes. Operators were blinded to mouse genotypes when inducing surgical injury models.

## Pharmacological inhibition of ferroptosis

Mice were randomly assigned to vehicle (1% dimethyl sulfoxide in phosphate-buffered saline) and liproxstatin-1 (10 mg/kg, Selleckchem, S7699, *Friedmann Angeli et al., 2014*) groups. Liproxstatin-1 and vehicle were administered daily by intraperitoneal injections starting from 1 hr before renal ischemia. All the mice were subjected to the same ischemic stress (22 min ischemic time, unilateral IRI model) and tamoxifen treatment. The mice were euthanized, and kidneys were harvested on day 21 after IRI.

## Droplet-based scRNA-seq

Mice were transcardially perfused with ice-cold PBS, and the kidneys were harvested. The kidneys were dissociated with liberase TM (0.3 mg/mL, Roche, Basel, Switzerland, #291963), hyaluronidase (10  $\mu$ g/mL, Sigma, H4272), DNaseI (20  $\mu$ g/mL) at 37°C for 40 min, followed by incubation with 0.25% trypsin EDTA at 37°C for 30 min. Trypsin was inactivated using 10% fetal bovine serum in PBS. Cells were then resuspended in PBS supplemented with 0.01% bovine serum albumin. Our protocol yielded high cell viability (>95%) and very few doublets, enabling us to avoid the use of flow cytometry-based cell sorting. After filtration through a 40  $\mu$ m strainer, cells at a concentration of 100 cells/ $\mu$ l were run through microfluidic channels along with mRNA capture beads and droplet-generating oil, as previously described (*Kobayashi et al., 2020; Macosko et al., 2015*). cDNA libraries were generated and sequenced using HiSeq X Ten with 150 bp paired-end sequencing. Each condition contains the cells from three mice to minimize potential biological and technical variability.

## Data preprocessing, unsupervised clustering, and cell type annotation of Drop-Seq data

Analysis of the scRNA-seq of mouse kidneys was performed by processing FASTQ files using drop-SeqPipe v0.3 and mapped on the GRCh38 genome reference with annotation version 91. Unique molecular identifier (UMI) counts were then further analyzed using an R package Seurat v.3.06 for quality control, dimensionality reduction, and cell clustering (Stuart et al., 2019). The scRNA-seq matrices were filtered by custom cutoff (genes expressed in >3 cells and cells expressing more than 500 and less than 3000 detected genes were included) to remove potential empty droplets and doublets. Relationships between the number of UMI/cell and genes/cell were comparable across the condition (Figure 1—figure supplement 3A). After quality control filtration and normalization using SCTransform (Hafemeister and Satija, 2019), UMI count matrices from post-IRI kidneys and homeostatic kidneys were integrated using Seurat's integration and label transfer method, which corrects potential batch effects (Stuart et al., 2019). The integrated dataset was used for all the analyses. To remove an additional confounding source of variation, the mitochondrial mapping percentage was regressed out. The number of principal components (PC) for downstream analyses were determined using elbow plot to identify knee point, and we included the first 25 PCs for the downstream analyses. A graph-based clustering approach in Seurat was used to cluster the cells in our integrated dataset. The resolution was set at 1.0 for the mouse integrated dataset. Cluster-defining markers for each cluster were obtained using the Seurat FindAllMarkers command (genes at least expressed in 25% of cells within the cluster, log fold change > 0.25) with the Wilcoxon Rank Sum test (Supplementary file 1). Based on the marker genes and manual curation of the gene expression pattern of canonical marker genes in UMAP plots (Figure 1—figure supplement 4), we assigned a cell identity to each cluster. Ambiguous clusters were shown as unknown. We manually combined 3 clusters of differentiated proximal tubular cells (PT, S1/S2 and PT, S2/S3; Figure 1—figure supplement 4) into one cluster (PT) to generate a more coarse-grained cell-type annotation and data visualization. We also combined three clusters of endothelial cells (Endo-1, Endo-2, and Endo-3; Figure 1—figure supplement 4) into one cluster (Endo) for data visualization.

## Data preprocessing, unsupervised clustering, and cell type annotation of mouse neonatal kidneys

The RDS files for mouse neonatal kidneys (postnatal day 1) were obtained from Gene Expression Omnibus (GEO accession number: GSE94333, GSM2473317), (Adam et al., 2017). Data were analyzed as in our mouse kidney dataset using Seurat and SCTransform (Stuart et al., 2019; Hafemeister and Satija, 2019). We included the first 17 PCs for the downstream analyses of mouse neonatal kidneys. A graph-based clustering approach in Seurat was used to cluster the cells. The resolution was set at 0.8. Based on the marker genes and manual curation of the gene expression pattern of canonical marker genes in UMAP plots (Figure 1—figure supplement 7), we assigned a cell identity to each cluster. The anchor genes for assigning cell identity were obtained from previous single-cell transcriptome analyses of the developing mouse kidneys (Adam et al., 2017; Combes et al., 2019b).

## Data preprocessing, unsupervised clustering, and cell type annotation of human kidneys

The RDS files for human kidneys were obtained from Gene Expression Omnibus (GEO accession number: GSE131882 and GSE145927), (Malone et al., 2020; Wilson et al., 2019). Normal human kidney data was originated from two macroscopically normal nephrectomy samples without renal mass (GSE131882; GSM3823939 and GSM3823941), (Wilson et al., 2019). Human AKI kidney data was originated from two biopsy-samples of transplant kidneys with evidence of AKI and acute tubular injury but no evidence of rejection (GSE145927; GSM4339775 and GSM4339778), (Malone et al., 2020). Data were integrated and analyzed as in the mouse kidney analyses using Seurat's integration method and SCTransform (Stuart et al., 2019; Hafemeister and Satija, 2019). We included the first 25 PCs for the downstream analyses of human normal and AKI kidneys. A graph-based clustering approach in Seurat was used to cluster the cells. The resolution was set at 0.5 for normal human kidneys and 1.0 for the human AKI kidneys. Based on the marker genes and manual curation of the gene expression pattern of canonical marker genes in UMAP plots (Figure 5—figure supplement 2

and **Figure 6—figure supplement 1**), we assigned a cell identity to each cluster. The anchor genes for assigning cell identity were obtained from previous single-cell transcriptome analyses of the human kidneys (Malone et al., 2020; Wilson et al., 2019; Stewart et al., 2019).

### Differential gene expression analyses and Gene ontology (GO) enrichment analyses

To predict the cellular functions based on enriched gene signature, we performed gene-ontology enrichment analyses. Differentially expressed genes obtained using FindMarkers command in Seurat were used for identifying signaling pathways and gene ontology through Enricher (Supplementary file 2 and 3; Figure 1—figure supplement 5B), (Kuleshov et al., 2016). To visualize the overrepresented signaling pathways, scaled data in the integrated Seurat object were extracted. Then, mean values of the scaled score of gene members in each GO class were calculated and shown in UMAP (Kobayashi et al., 2020). The gene member lists of signaling pathways were obtained from AmiGO 2 (AmiGO Hub et al., 2009). Log<sub>2</sub> fold changes and P-values of each gene extracted using FindMarkers command in Seurat with Wilcoxon rank sum test were shown in a volcano plot using an R package EnhancedVolcano v1.4.0 (Blighe et al., 2021; <https://github.com/kevinblighe/EnhancedVolcano>), (Figure 1—figure supplement 5B). Top 100 genes in mature and early PT cell clusters were obtained using the 'FindMarkers' command in Seurat. These genes were visualized on the UMAP plots using the scaled score as in GO class visualization.

### RNA velocity analyses

To infer future states of individual cells, we performed RNA velocity analyses (La Manno et al., 2018) using single-time point dataset of post-IRI kidney on day 7. The aligned BAM files were used as input for Velocyto to obtain the counts of unspliced and spliced reads in loom format. Cell barcodes for the clusters of interests (PT and DA-PT) were extracted and utilized for velocyto run command in velocyto.py v0.17.15, as well as for generating RNA velocity plots using velocyto.R v0.6 in combination with an R package SeuratWrappers v0.2.0 (Stuart et al., 2019; <https://github.com/satijalab/seurat-wrappers>). Twenty-five nearest neighbors in slope calculation smoothing were used for RunVelocity command.

### Pseudotime trajectory analyses

To infer the dynamic cellular process during injury and repair, we performed single-cell trajectory analyses. We first extracted the clusters of interests (PT and DA-PT) from our integrated Seurat object of mouse kidneys and utilized for Monocle 3 (version 0.2.3.0) analyses with default parameters to identify a pseudotime trajectory with SeuratWrappers v0.2.0 (Cao et al., 2019; Trapnell et al., 2014). We set the starting states in two different approaches. We used the UMAP space area occupied by cells from the earliest time point of IRI kidneys (6 hr post-IRI, Figure 1F) and the area occupied by the cells with high expression of genes that are highly expressed in differentiated PT cells, such as *Slc34a1* (Figure 1—figure supplement 8B) as the starting state, respectively. Both approaches resulted in similar trajectory inference. For the human AKI dataset, we extracted the clusters of interests (PT and DA-PT-like) from our integrated Seurat object and applied the Monocle 3 algorithm with default parameters. We used the UMAP space area occupied by the cells with high expression of homeostatic genes (*ALDOB*), (Figure 6F).

### Intercellular communication analyses using NicheNet

To predict the intercellular communication process between damage-associated PT (DA-PT) cells and myeloid cells (monocytes and macrophages), we performed NicheNet analyses based on the analytical pipeline (Browaeys et al., 2020; [https://github.com/saeyslab/nichenetr/blob/master/vignettes/seurat\\_wrapper.md](https://github.com/saeyslab/nichenetr/blob/master/vignettes/seurat_wrapper.md)) using an R package nichenetr (version 1.0.0) with default parameters (Browaeys et al., 2020). Based on high enrichment of chemokines and cytokines in DA-PT cells and the observed positive association between the numbers of macrophages and DA-PT cells in severely injured kidneys, we surmised that they have a close molecular interaction. We used NicheNet to predict the ligand-receptor pairs that are most likely to explain the target gene expression in renal myeloid cells after IRI. We defined DA-PT cells as the 'sender/niche' cell population and myeloid cells as the 'receiver/target' cell population in our integrated Seurat object for these analyses. We defined



the differentially expressed genes in monocytes or macrophages in IRI-kidneys compared to homeostatic kidneys as the gene sets of interest that were affected by predicted ligand-receptor interactions.

## Tissue collection and histology

Kidneys were prepared as described previously (Nezu *et al.*, 2017; Ide *et al.*, 2020). For cryosections (7  $\mu\text{m}$ ), the tissues were fixed with 4% paraformaldehyde in PBS at 4°C for 4 hr and then processed through a sucrose gradient. Kidneys were embedded in OCT compound for sectioning. For paraffin sections (5  $\mu\text{m}$ ), the tissues were fixed with 10% neutral buffered formalin overnight at 4°C and processed at Substrate Services Core and Research Support at Duke. Sections were blocked (animal-free blocker with 0.5% triton x-100) for 30 min and incubated with the primary antibodies overnight at 4°C. Primary antibodies used were as follows: SOX9 (Abcam, Cambridge, UK, ab196450 or ab185966, 1:200), KIM1 (R and D Systems, Minneapolis, MN, AF1817, 1:400), NGAL (Abcam, ab70287, 1:400), F4/80 (Bio-rad, Hercules, CA, MCA497G, 1:200),  $\alpha$ -SMA (Sigma, C6198, 1:200), LTL (Vector, Burlingame, CA, B-1325 or FL-1321, 1:200), KRT8 (DSHB, TROMA-I, 1:200), MDA (Abcam, ab6463, 1:200), ACSL4 (Abcam, ab204380 or ab155282, 1:200), EMN (Abcam, 106100, 1:200), VCAM1 (CST, 39036S or 33901S, 1:100), and GPX4 (Abcam, ab125066, 1:200). Alexa Fluor-labeled secondary antibodies were used appropriately for immunofluorescence. ImmPRES HRP reagent kit was used for immunohistochemistry (Vector, MP-7401). Nuclei were stained with DAPI (1:400, Sigma). Heat-induced antigen retrieval was performed using pH 6.0 sodium citrate solution (eBioscience). Experiments for RNAScope in situ hybridization (Advanced Cell Diagnostics, ACD, Newark, CA) was performed as recommended by the manufacturer. Mm-Cdh6 (ACD, 519541) was used. Images were captured using Axio imager and 780 confocal microscopes (Zeiss, Oberkochen, Germany). Paraffin-sections were stained with hematoxylin and eosin (H and E). The kidney injury score was calculated as we previously reported (Ren *et al.*, 2020). TUNEL staining was performed following the manufacturer's instruction (Abcam, ab206386). To ensure the TUNEL signal's specificity, we used sections treated with DNase I as a positive control and a section treated without terminal deoxynucleotidyl transferase as a negative control, as recommended by the manufacturer. Sections were counterstained with methyl green. More than three randomly selected areas from at least three kidneys were imaged and quantified using ImageJ (Ide *et al.*, 2020). The stitched large area was used for quantification to alleviate the selection bias in the acquisition of images. All representative images were from more than three kidneys tested.

## RNA extraction and real-time quantitative PCR

Total RNA was extracted from kidneys using the TRIzol reagent (Invitrogen, 15596026). Three  $\mu\text{g}$  of total RNA was then reverse transcribed with Maxima H minus cDNA synthesis master mix (Invitrogen, M1662). Equivalent amounts of diluted cDNA from each sample were analyzed with Real-time PCR with the primers listed below using the Powerup SYBR Green reagent (Invitrogen, A25776) on a QuantStudio three real-time PCR systems (Thermo). 18S rRNA expression was used to normalize samples using the  $\Delta\Delta\text{CT}$ -method.

## Statistical analysis

Statistical analyses were conducted using GraphPad Prism software. Two-tailed unpaired Student's t-test was used for two groups, and one-way analysis of variance (ANOVA) followed by Sidak multiple comparison test was used for more than two groups. All results are represented as means  $\pm$  SE. A p value less than 0.05 was considered statistically significant.

Additional protocols are available in the supplementary method.

Primers used for quantitative PCR.

Sox9: Fw-GAGCCGGATCTGAAGAGGGA, Rv-GCTTGACGTGTGGCTTGTTCC  
Vcam1: Fw-TCTTACCTGTGCGCTGTGAC, Rv-ACTGGATCTTCAGGGAATGAGT  
Cdh6: Fw-CCAATATTCACCAAGGACGTTTA, Rv-CGTGACTTGGACCACAAATG  
Acsm2: Fw-CCAAGATGGCAGAACACTCC, Rv-TCAGAAGTACTCAGGCCTGTCC  
Icam1: Fw-GCTACCATCACCGTGTATTCG, Rv-AGGTCCTTGCCTACTTGCTG  
Pdgfb: Fw-CGAGGGAGGAGGAGCCTA, Rv-GTCTTGCCTCGGCGATTA  
ApoE: Fw-TTGGTACATTGCTGACAGG, Rv-AGCGCAGGTAATCCAGAA  
Havcr1: Fw-AAACCAGAGATTCCCACACG, Rv-GTCGTGGGTCTTCTGTAGC

*Lcn2*: Fw-CAAGCAATACTTCAAAATTACCCTGTA, Rv-GCAAAGCGGGTGAAACGTT  
*Acta2*: Fw-CCCACCCAGAGTGGAGAA, Rv-ACATAGCTGGAGCAGCGTCT  
*Slc34a1*: Fw-CTCATTTCGGATTTGGTGTCA, Rv-GGCCTCTACCCTGGACATAGA  
*Krt8*: Fw-CTGAGCTTGGCAACATGC, Rv-ACGCTTGTTGATCTCATCCTC  
*18S rRNA*: Fw-CGGCTACCACATCCAAGGAA, Rv-GCTGGAATTACCGCGGCT

Genotyping primers.

*Cre*, Fw: GTGCAAGTTGAATAACCGGAAATGG,  
*Cre*, Rv: AGAGTCATCCTTAGCGCCGTAATCAAT  
*Gpx4<sup>flox</sup>*, wt: CTGCAACAGCTCCGAGTTC  
*Gpx4<sup>flox</sup>*, common: CGGTGCCAAAGAAAGAAAGT  
*Gpx4<sup>flox</sup>*, mut: CCAGTAAGCAGTGGGTTCTC  
*Rosa26<sup>tdTomato</sup>*, Fw: CTGTTCTGTACGGCATGG  
*Rosa26<sup>tdTomato</sup>*, Rv-GGCATTAAGCAGCGTATCC  
*Rosa26<sup>wt</sup>*, Fw: AAGGGAGCTGCAGTGGAGTA  
*Rosa26<sup>wt</sup>*, Rv: CCGAAAATCTGTGGGAAGTC.

## Acknowledgements

We thank Drs. Brigid Hogan and Myles Wolf for critical advice and helpful suggestions on the manuscript. We also thank Dr. Helene F Kirshner (Duke Center for Genomic and Computational Biology) for her bioinformatical support on our single-cell transcriptome dataset. The monoclonal antibody against keratin 8 (TROMA-1, developed by Drs. P Brulet and R Kemeler) was obtained from the Developmental Studies Hybridoma Bank, created by the NICHD of the NIH and maintained at the Department of Biology, The University of Iowa. We thank Drs. Tetsuhiro Yokonishi (Duke University), Leslie Gewin and Kensei Taguchi (Vanderbilt University), and members of the Crowley lab for their technical advice. This study was supported by grants from the National Institute of Diabetes and Digestive and Kidney Diseases (R01 DK123097), a pilot award from the Northwestern University George M O'Brien Kidney Research Core Center (P30 DK114857), the American Society of Nephrology Carl W Gottschalk Career Developmental Grant, and Duke Nephrology Start-up Fund to TS. SI, YK, and KI are supported in part by fellowship grants from the American Heart Association, Japan Society for the Promotion of Science, and the Astellas Foundation for Research on Metabolic Disorders, respectively. Imaging was performed at the Duke Light Microscopy Core Facility supported by the shared instrumentation grant (1S10RR027528-01).

## Additional information

### Funding

Funder	Grant reference number	Author
National Institute of Diabetes and Digestive and Kidney Diseases	R01 DK123097	Tomokazu Souma
National Institute of Diabetes and Digestive and Kidney Diseases	P30 DK114857	Tomokazu Souma
American Society of Nephrology		Tomokazu Souma
American Heart Association	20POST35210465	Shintaro Ide
Astellas Foundation for Research on Metabolic Disorders		Kana Ide
Japan Society for the Promotion of Science		Yoshihiko Kobayashi

The funders had no role in study design, data collection and interpretation, or the decision to submit the work for publication.

**Author contributions**

Shintaro Ide, Formal analysis, Investigation, Writing - original draft, Writing - review and editing; Yoshihiko Kobayashi, Formal analysis, Investigation, Methodology, Writing - review and editing; Kana Ide, Formal analysis, Investigation, Project administration, Writing - review and editing; Sarah A Strausser, Investigation, Project administration, Writing - review and editing; Koki Abe, Formal analysis, Investigation; Savannah Herbek, Investigation, Writing - review and editing; Lori L O'Brien, Formal analysis, Writing - review and editing; Steven D Crowley, Methodology, Writing - review and editing; Laura Barisoni, Resources, Writing - review and editing; Aleksandra Tata, Resources, Methodology, Writing - review and editing; Purushothama Rao Tata, Resources, Supervision, Methodology, Writing - review and editing; Tomokazu Souma, Conceptualization, Formal analysis, Supervision, Funding acquisition, Investigation, Writing - original draft, Project administration, Writing - review and editing

**Author ORCIDs**

Shintaro Ide  <https://orcid.org/0000-0002-9301-211X>

Kana Ide  <http://orcid.org/0000-0002-2845-8481>

Lori L O'Brien  <http://orcid.org/0000-0002-0741-181X>

Steven D Crowley  <http://orcid.org/0000-0002-1838-0561>

Purushothama Rao Tata  <http://orcid.org/0000-0003-4837-0337>

Tomokazu Souma  <https://orcid.org/0000-0002-3285-8613>

**Ethics**

Animal experimentation: All animal experiments were approved by the Institutional Animal Care and Use Committee at Duke University and performed according to the IACUC-approved protocols (A051-18-02 and A014-21-01) and adhered to the NIH Guide for the Care and Use of Laboratory.

**Decision letter and Author response**

Decision letter <https://doi.org/10.7554/eLife.68603.sa1>

Author response <https://doi.org/10.7554/eLife.68603.sa2>

**Additional files****Supplementary files**

- Supplementary file 1. Cluster-enriched genes in **Figure 1**.
- Supplementary file 2. Differentially expressed genes in PT cells.
- Supplementary file 3. Gene ontology analyses of PT cells.
- Transparent reporting form

**Data availability**

Sequencing data have been deposited in GEO under accession codes GSE161201.

The following dataset was generated:

Author(s)	Year	Dataset title	Dataset URL	Database and Identifier
Ide S, Kobayashi Y, Ide K, Strausser SA, Herbek S, O'Brien LL, Crowley SD, Barisoni L, Tata A, Tata PR, Soum T	2020	Ferroptotic stress promotes the accumulation of pro-inflammatory proximal tubular cells in maladaptive renal repair	<a href="https://www.ncbi.nlm.nih.gov/geo/query/acc.cgi?acc=GSE161201">https://www.ncbi.nlm.nih.gov/geo/query/acc.cgi?acc=GSE161201</a>	NCBI Gene Expression Omnibus, GSE161201

The following previously published datasets were used:

Author(s)	Year	Dataset title	Dataset URL	Database and Identifier
Adam M, Potter SS	2017	The use of cold active proteases can dramatically reduce single cell RNA-seq gene expression artifacts	<a href="https://www.ncbi.nlm.nih.gov/geo/query/acc.cgi?acc=GSE94333">https://www.ncbi.nlm.nih.gov/geo/query/acc.cgi?acc=GSE94333</a>	NCBI Gene Expression Omnibus, GSE94333
Wilson PC, Humphreys BD	2019	The Single Cell Transcriptomic Landscape of Early Human Diabetic Nephropathy	<a href="https://www.ncbi.nlm.nih.gov/geo/query/acc.cgi?acc=GSE131882">https://www.ncbi.nlm.nih.gov/geo/query/acc.cgi?acc=GSE131882</a>	NCBI Gene Expression Omnibus, GSE131882
Malone AF	2020	Single Cell Transcriptional Analysis of Donor and Recipient Immune Cell Chimerism in the Rejecting Kidney Transplant	<a href="https://www.ncbi.nlm.nih.gov/geo/query/acc.cgi?acc=GSE145927">https://www.ncbi.nlm.nih.gov/geo/query/acc.cgi?acc=GSE145927</a>	NCBI Gene Expression Omnibus, GSE145927

## References

- Adam M, Potter AS, Potter SS. 2017. Psychrophilic proteases dramatically reduce single-cell RNA-seq artifacts: a molecular atlas of kidney development. *Development* **144**:3625–3632. DOI: <https://doi.org/10.1242/dev.151142>, PMID: 28851704
- Alim I, Caulfield JT, Chen Y, Swarup V, Geschwind DH, Ivanova E, Seravalli J, Ai Y, Sansing LH, Ste Marie EJ, Hondal RJ, Mukherjee S, Cave JW, Sagdullaev BT, Karuppagounder SS, Ratan RR. 2019. Selenium drives a transcriptional adaptive program to block ferroptosis and treat stroke. *Cell* **177**:1262–1279. DOI: <https://doi.org/10.1016/j.cell.2019.03.032>, PMID: 31056284
- AmiGO Hub, Web Presence Working Group, Carbon S, Ireland A, Mungall CJ, Shu S, Marshall B, Lewis S. 2009. AmiGO: online access to ontology and annotation data. *Bioinformatics* **25**:288–289. DOI: <https://doi.org/10.1093/bioinformatics/btn615>, PMID: 19033274
- Berger K, Bangen JM, Hammerich L, Liedtke C, Floege J, Smeets B, Moeller MJ. 2014. Origin of regenerating tubular cells after acute kidney injury. *PNAS* **111**:1533–1538. DOI: <https://doi.org/10.1073/pnas.1316177111>, PMID: 24474779
- Blighe K, Rana S, Lewis M. 2021. EnhancedVolcano: Publication-ready volcano plots with enhanced colouring and labeling. *R Package Version 1.10.0*. <https://github.com/kevinblighe/EnhancedVolcano>
- Browaeys R, Saelens W, Saeys Y. 2020. NicheNet: modeling intercellular communication by linking ligands to target genes. *Nature Methods* **17**:159–162. DOI: <https://doi.org/10.1038/s41592-019-0667-5>, PMID: 31819264
- Canaud G, Brooks CR, Kishi S, Taguchi K, Nishimura K, Magassa S, Scott A, Hsiao LL, Ichimura T, Terzi F, Yang L, Bonventre JV. 2019. Cyclin G1 and TASC2 regulate kidney epithelial cell G2-M arrest and fibrotic maladaptive repair. *Science Translational Medicine* **11**:eaav4754. DOI: <https://doi.org/10.1126/scitranslmed.aav4754>, PMID: 30674655
- Cao J, Spielmann M, Qiu X, Huang X, Ibrahim DM, Hill AJ, Zhang F, Mundlos S, Christiansen L, Steemers FJ, Trapnell C, Shendure J. 2019. The single-cell transcriptional landscape of mammalian organogenesis. *Nature* **566**:496–502. DOI: <https://doi.org/10.1038/s41586-019-0969-x>, PMID: 30787437
- Chawla LS, Amdur RL, Amodeo S, Kimmel PL, Palant CE. 2011. The severity of acute kidney injury predicts progression to chronic kidney disease. *Kidney International* **79**:1361–1369. DOI: <https://doi.org/10.1038/ki.2011.42>, PMID: 21430640
- Chawla LS, Eggers PW, Star RA, Kimmel PL. 2014. Acute kidney injury and chronic kidney disease as interconnected syndromes. *New England Journal of Medicine* **371**:58–66. DOI: <https://doi.org/10.1056/NEJMr1214243>, PMID: 24988558
- Cho EA, Patterson LT, Brookhiser WT, Mah S, Kintner C, Dressler GR. 1998. Differential expression and function of cadherin-6 during renal epithelium development. *Development* **125**:803–812. DOI: <https://doi.org/10.1242/dev.125.5.803>, PMID: 9449663
- Choi J, Park JE, Tsagkogeorga G, Yanagita M, Koo BK, Han N, Lee JH. 2020. Inflammatory signals induce AT2 Cell-Derived Damage-Associated transient progenitors that mediate alveolar regeneration. *Cell Stem Cell* **27**:366–382. DOI: <https://doi.org/10.1016/j.stem.2020.06.020>, PMID: 32750316
- Cippà PE, Sun B, Liu J, Chen L, Naesens M, McMahon AP. 2018. Transcriptional trajectories of human kidney injury progression. *JCI Insight* **3**:123151. DOI: <https://doi.org/10.1172/jci.insight.123151>, PMID: 30429361
- Combes AN, Zappia L, Er PX, Oshlack A, Little MH. 2019a. Single-cell analysis reveals congruence between kidney organoids and human fetal kidney. *Genome Medicine* **11**:3. DOI: <https://doi.org/10.1186/s13073-019-0615-0>, PMID: 30674341
- Combes AN, Phipson B, Lawlor KT, Dorison A, Patrick R, Zappia L, Harvey RP, Oshlack A, Little MH. 2019b. Single cell analysis of the developing mouse kidney provides deeper insight into marker gene expression and ligand-receptor crosstalk. *Development* **146**:dev178673. DOI: <https://doi.org/10.1242/dev.182162>, PMID: 31118232
- Daniels BP, Snyder AG, Olsen TM, Orozco S, Oguin TH, Tait SWG, Martinez J, Gale M, Loo YM, Oberst A. 2017. RIPK3 restricts viral pathogenesis via cell Death-Independent neuroinflammation. *Cell* **169**:301–313. DOI: <https://doi.org/10.1016/j.cell.2017.03.011>, PMID: 28366204

- Dickman KG**, Sweet DH, Bonala R, Ray T, Wu A. 2011. Physiological and molecular characterization of aristolochic acid transport by the kidney. *Journal of Pharmacology and Experimental Therapeutics* **338**:588–597. DOI: <https://doi.org/10.1124/jpet.111.180984>, PMID: 21546538
- Dixon SJ**, Lemberg KM, Lamprecht MR, Skouta R, Zaitsev EM, Gleason CE, Patel DN, Bauer AJ, Cantley AM, Yang WS, Morrison B, Stockwell BR. 2012. Ferroptosis: an iron-dependent form of nonapoptotic cell death. *Cell* **149**:1060–1072. DOI: <https://doi.org/10.1016/j.cell.2012.03.042>, PMID: 22632970
- Doll S**, Proneth B, Tyurina YY, Panzilius E, Kobayashi S, Ingold I, Irmeler M, Beckers J, Aichler M, Walch A, Prokisch H, Trümbach D, Mao G, Qu F, Bayir H, Füllekrug J, Scheel CH, Wurst W, Schick JA, Kagan VE, et al. 2017. ACSL4 dictates ferroptosis sensitivity by shaping cellular lipid composition. *Nature Chemical Biology* **13**:91–98. DOI: <https://doi.org/10.1038/nchembio.2239>, PMID: 27842070
- Famulski KS**, de Freitas DG, Kreepala C, Chang J, Sellares J, Sis B, Einecke G, Mengel M, Reeve J, Halloran PF. 2012. Molecular phenotypes of acute kidney injury in kidney transplants. *Journal of the American Society of Nephrology* **23**:948–958. DOI: <https://doi.org/10.1681/ASN.2011090887>, PMID: 22343120
- Ferenbach DA**, Bonventre JV. 2015. Mechanisms of maladaptive repair after AKI leading to accelerated kidney ageing and CKD. *Nature Reviews Nephrology* **11**:264–276. DOI: <https://doi.org/10.1038/nrneph.2015.3>, PMID: 25643664
- Friedmann Angeli JP**, Schneider M, Proneth B, Tyurina YY, Tyurin VA, Hammond VJ, Herbach N, Aichler M, Walch A, Eggenhofer E, Basavarajappa D, Rådmark O, Kobayashi S, Seibt T, Beck H, Neff F, Esposito I, Wanke R, Förster H, Yefremova O, et al. 2014. Inactivation of the ferroptosis regulator Gpx4 triggers acute renal failure in mice. *Nature Cell Biology* **16**:1180–1191. DOI: <https://doi.org/10.1038/ncb3064>, PMID: 25402683
- Fu Y**, Tang C, Cai J, Chen G, Zhang D, Dong Z. 2018. Rodent models of AKI-CKD transition. *American Journal of Physiology-Renal Physiology* **315**:F1098–F1106. DOI: <https://doi.org/10.1152/ajprenal.00199.2018>, PMID: 29949392
- Furuyama K**, Kawaguchi Y, Akiyama H, Horiguchi M, Kodama S, Kuhara T, Hosokawa S, Elbahrawy A, Soeda T, Koizumi M, Masui T, Kawaguchi M, Takaori K, Doi R, Nishi E, Kakinoki R, Deng JM, Behringer RR, Nakamura T, Uemoto S. 2011. Continuous cell supply from a Sox9-expressing progenitor zone in adult liver, exocrine pancreas and intestine. *Nature Genetics* **43**:34–41. DOI: <https://doi.org/10.1038/ng.722>, PMID: 21113154
- Gewin LS**. 2018. Renal fibrosis: primacy of the proximal tubule. *Matrix Biology* **68–69**:248–262. DOI: <https://doi.org/10.1016/j.matbio.2018.02.006>, PMID: 29425694
- Hafemeister C**, Satija R. 2019. Normalization and variance stabilization of single-cell RNA-seq data using regularized negative binomial regression. *Genome Biology* **20**:296. DOI: <https://doi.org/10.1186/s13059-019-1874-1>, PMID: 31870423
- Hauser IA**, Riess R, Hausknecht B, Thüringer H, Sterzel RB. 1997. Expression of cell adhesion molecules in primary renal disease and renal allograft rejection. *Nephrology Dialysis Transplantation* **12**:1122–1131. DOI: <https://doi.org/10.1093/ndt/12.6.1122>, PMID: 9198039
- Hsu CC**, Kao WH, Coresh J, Pankow JS, Marsh-Manzi J, Boerwinkle E, Bray MS. 2005. Apolipoprotein E and progression of chronic kidney disease. *Jama* **293**:2892–2899. DOI: <https://doi.org/10.1001/jama.293.23.2892>, PMID: 15956634
- Humphreys BD**. 2018. Mechanisms of renal fibrosis. *Annual Review of Physiology* **80**:309–326. DOI: <https://doi.org/10.1146/annurev-physiol-022516-034227>, PMID: 29068765
- Ichimura T**, Asseldonk EJ, Humphreys BD, Gunaratnam L, Duffield JS, Bonventre JV. 2008. Kidney injury molecule-1 is a phosphatidylserine receptor that confers a phagocytic phenotype on epithelial cells. *Journal of Clinical Investigation* **118**:1657–1668. DOI: <https://doi.org/10.1172/JCI34487>, PMID: 18414680
- Ide S**, Yahara Y, Kobayashi Y, Strausser SA, Ide K, Watwe A, Xu-Vanpala S, Privratsky JR, Crowley SD, Shinohara ML, Alman BA, Souma T. 2020. Yolk-sac-derived macrophages progressively expand in the mouse kidney with age. *eLife* **9**:e51756. DOI: <https://doi.org/10.7554/eLife.51756>, PMID: 32301704
- Kadaja M**, Keyes BE, Lin M, Pasolli HA, Genander M, Polak L, Stokes N, Zheng D, Fuchs E. 2014. SOX9: a stem cell transcriptional regulator of secreted niche signaling factors. *Genes & Development* **28**:328–341. DOI: <https://doi.org/10.1101/gad.233247.113>, PMID: 24532713
- Kagan VE**, Mao G, Qu F, Angeli JP, Doll S, Croix CS, Dar HH, Liu B, Tyurin VA, Ritov VB, Kapralov AA, Amoscato AA, Jiang J, Anthonymuthu T, Mohammadyani D, Yang Q, Proneth B, Klein-Seetharaman J, Watkins S, Bahar I, et al. 2017. Oxidized arachidonic and adrenic PEs navigate cells to ferroptosis. *Nature Chemical Biology* **13**:81–90. DOI: <https://doi.org/10.1038/nchembio.2238>, PMID: 27842066
- Kang HM**, Huang S, Reidy K, Han SH, Chinga F, Susztak K. 2016. Sox9-Positive progenitor cells play a key role in renal tubule epithelial regeneration in mice. *Cell Reports* **14**:861–871. DOI: <https://doi.org/10.1016/j.celrep.2015.12.071>, PMID: 26776520
- Kenny EM**, Fidan E, Yang Q, Anthonymuthu TS, New LA, Meyer EA, Wang H, Kochanek PM, Dixon CE, Kagan VE, Bayir H. 2019. Ferroptosis contributes to neuronal death and functional outcome after traumatic brain injury. *Critical Care Medicine* **47**:410–418. DOI: <https://doi.org/10.1097/CCM.0000000000003555>, PMID: 30531185
- Kirita Y**, Wu H, Uchimura K, Wilson PC, Humphreys BD. 2020. Cell profiling of mouse acute kidney injury reveals conserved cellular responses to injury. *PNAS* **117**:15874–15883. DOI: <https://doi.org/10.1073/pnas.2005477117>, PMID: 32571916
- Kishi S**, Brooks CR, Taguchi K, Ichimura T, Mori Y, Akinfolarin A, Gupta N, Galichon P, Elias BC, Suzuki T, Wang Q, Gewin L, Morizane R, Bonventre JV. 2019. Proximal tubule ATR regulates DNA repair to prevent maladaptive renal injury responses. *Journal of Clinical Investigation* **129**:4797–4816. DOI: <https://doi.org/10.1172/JCI122313>, PMID: 31589169

- Kobayashi Y**, Tata A, Konkimalla A, Katsura H, Lee RF, Ou J, Banovich NE, Kropski JA, Tata PR. 2020. Persistence of a regeneration-associated, transitional alveolar epithelial cell state in pulmonary fibrosis. *Nature Cell Biology* **22**:934–946. DOI: <https://doi.org/10.1038/s41556-020-0542-8>, PMID: 32661339
- Kuleshov MV**, Jones MR, Rouillard AD, Fernandez NF, Duan Q, Wang Z, Koplev S, Jenkins SL, Jagodnik KM, Lachmann A, McDermott MG, Monteiro CD, Gunderson GW, Ma'ayan A. 2016. Enrichr: a comprehensive gene set enrichment analysis web server 2016 update. *Nucleic Acids Research* **44**:W90–W97. DOI: <https://doi.org/10.1093/nar/gkw377>
- Kumar S**, Liu J, Pang P, Krautzberger AM, Reginensi A, Akiyama H, Schedl A, Humphreys BD, McMahon AP. 2015. Sox9 activation highlights a cellular pathway of renal repair in the acutely injured mammalian kidney. *Cell Reports* **12**:1325–1338. DOI: <https://doi.org/10.1016/j.celrep.2015.07.034>, PMID: 26279573
- Kusaba T**, Lalli M, Kramann R, Kobayashi A, Humphreys BD. 2014. Differentiated kidney epithelial cells repair injured proximal tubule. *PNAS* **111**:1527–1532. DOI: <https://doi.org/10.1073/pnas.1310653110>, PMID: 24127583
- La Manno G**, Soldatov R, Zeisel A, Braun E, Hochgerner H, Petukhov V, Lidschreiber K, Kastriti ME, Lönnerberg P, Furlan A, Fan J, Borm LE, Liu Z, van Bruggen D, Guo J, He X, Barker R, Sundström E, Castelo-Branco G, Cramer P, et al. 2018. RNA velocity of single cells. *Nature* **560**:494–498. DOI: <https://doi.org/10.1038/s41586-018-0414-6>, PMID: 30089906
- Ledo N**, Ko YA, Park AS, Kang HM, Han SY, Choi P, Susztak K. 2015. Functional genomic annotation of genetic risk loci highlights inflammation and epithelial biology networks in CKD. *Journal of the American Society of Nephrology* **26**:692–714. DOI: <https://doi.org/10.1681/ASN.2014010028>, PMID: 25231882
- Legouis D**, Ricksten SE, Faivre A, Verissimo T, Gariani K, Verney C, Galichon P, Berchtold L, Feraille E, Fernandez M, Placier S, Koppitch K, Hertig A, Martin PY, Naesens M, Pugin J, McMahon AP, Cippà PE, de Seigneux S. 2020. Altered proximal tubular cell glucose metabolism during acute kidney injury is associated with mortality. *Nature Metabolism* **2**:732–743. DOI: <https://doi.org/10.1038/s42255-020-0238-1>, PMID: 32694833
- Lewington AJ**, Cerdá J, Mehta RL. 2013. Raising awareness of acute kidney injury: a global perspective of a silent killer. *Kidney International* **84**:457–467. DOI: <https://doi.org/10.1038/ki.2013.153>, PMID: 23636171
- Li Y**, Feng D, Wang Z, Zhao Y, Sun R, Tian D, Liu D, Zhang F, Ning S, Yao J, Tian X. 2019. Ischemia-induced ACSL4 activation contributes to ferroptosis-mediated tissue injury in intestinal ischemia/reperfusion. *Cell Death & Differentiation* **26**:2284–2299. DOI: <https://doi.org/10.1038/s41418-019-0299-4>, PMID: 30737476
- Linkermann A**, Skouta R, Himmerkus N, Mulay SR, Dewitz C, De Zen F, Prokai A, Zuchtriegel G, Krombach F, Welz PS, Weinlich R, Vanden Berghe T, Vandenabeele P, Pasparakis M, Bleich M, Weinberg JM, Reichel CA, Bräsen JH, Kunzendorf U, Anders HJ, et al. 2014. Synchronized renal tubular cell death involves ferroptosis. *PNAS* **111**:16836–16841. DOI: <https://doi.org/10.1073/pnas.1415518111>, PMID: 25385600
- Liu J**, Kumar S, Dolzhenko E, Alvarado GF, Guo J, Lu C, Chen Y, Li M, Dessing MC, Parvez RK, Cippà PE, Krautzberger AM, Saribekyan G, Smith AD, McMahon AP. 2017. Molecular characterization of the transition from acute to chronic kidney injury following ischemia/reperfusion. *JCI Insight* **2**:e94716. DOI: <https://doi.org/10.1172/jci.insight.94716>
- Macosko EZ**, Basu A, Satija R, Nemes J, Shekhar K, Goldman M, Tirosh I, Bialas AR, Kamitaki N, Martersteck EM, Trombetta JJ, Weitz DA, Sanes JR, Shalek AK, Regev A, McCarroll SA. 2015. Highly parallel Genome-wide expression profiling of individual cells using nanoliter droplets. *Cell* **161**:1202–1214. DOI: <https://doi.org/10.1016/j.cell.2015.05.002>, PMID: 26000488
- Madisen L**, Zwingman TA, Sunkin SM, Oh SW, Zariwala HA, Gu H, Ng LL, Palmiter RD, Hawrylycz MJ, Jones AR, Lein ES, Zeng H. 2010. A robust and high-throughput cre reporting and characterization system for the whole mouse brain. *Nature Neuroscience* **13**:133–140. DOI: <https://doi.org/10.1038/nn.2467>, PMID: 20023653
- Mah SP**, Saueressig H, Goulding M, Kintner C, Dressler GR. 2000. Kidney development in cadherin-6 mutants: delayed mesenchyme-to-epithelial conversion and loss of nephrons. *Developmental Biology* **223**:38–53. DOI: <https://doi.org/10.1006/dbio.2000.9738>, PMID: 10864459
- Malone AF**, Wu H, Fronick C, Fulton R, Gaut JP, Humphreys BD. 2020. Harnessing expressed single nucleotide variation and single cell RNA sequencing to define immune cell chimerism in the rejecting kidney transplant. *Journal of the American Society of Nephrology* **31**:1977–1986. DOI: <https://doi.org/10.1681/ASN.2020030326>, PMID: 32669324
- Marable SS**, Chung E, Adam M, Potter SS, Park JS. 2018. Hnf4a deletion in the mouse kidney phenocopies fanconi renotubular syndrome. *JCI Insight* **3**:e97497. DOI: <https://doi.org/10.1172/jci.insight.97497>, PMID: 30046000
- Marable SS**, Chung E, Park JS. 2020. Hnf4a is required for the development of Cdh6-Expressing progenitors into proximal tubules in the mouse kidney. *Journal of the American Society of Nephrology* **31**:2543–2558. DOI: <https://doi.org/10.1681/ASN.2020020184>, PMID: 32764140
- Moriwaki K**, Balaji S, McQuade T, Malhotra N, Kang J, Chan FK. 2014. The necroptosis adaptor RIPK3 promotes injury-induced cytokine expression and tissue repair. *Immunity* **41**:567–578. DOI: <https://doi.org/10.1016/j.immuni.2014.09.016>, PMID: 25367573
- Moriwaki K**, Chan FK. 2016. Necroptosis-independent signaling by the RIP kinases in inflammation. *Cellular and Molecular Life Sciences* **73**:2325–2334. DOI: <https://doi.org/10.1007/s00018-016-2203-4>, PMID: 27048814
- Müller T**, Dewitz C, Schmitz J, Schröder AS, Bräsen JH, Stockwell BR, Murphy JM, Kunzendorf U, Krautwald S. 2017. Necroptosis and ferroptosis are alternative cell death pathways that operate in acute kidney failure. *Cellular and Molecular Life Sciences* **74**:3631–3645. DOI: <https://doi.org/10.1007/s00018-017-2547-4>, PMID: 28551825

- Nezu M**, Souma T, Yu L, Suzuki T, Saigusa D, Ito S, Suzuki N, Yamamoto M. 2017. Transcription factor Nrf2 hyperactivation in early-phase renal ischemia-reperfusion injury prevents tubular damage progression. *Kidney International* **91**:387–401. DOI: <https://doi.org/10.1016/j.kint.2016.08.023>, PMID: 27789056
- Paragas N**, Qiu A, Zhang Q, Samstein B, Deng SX, Schmidt-Ott KM, Viltard M, Yu W, Forster CS, Gong G, Liu Y, Kulkarni R, Mori K, Kalandadze A, Ratner AJ, Devarajan P, Landry DW, D'Agati V, Lin CS, Barasch J. 2011. The ngal reporter mouse detects the response of the kidney to injury in real time. *Nature Medicine* **17**:216–222. DOI: <https://doi.org/10.1038/nm.2290>, PMID: 21240264
- Park J**, Shrestha R, Qiu C, Kondo A, Huang S, Werth M, Li M, Barasch J, Suszták K. 2018. Single-cell transcriptomics of the mouse kidney reveals potential cellular targets of kidney disease. *Science* **360**:758–763. DOI: <https://doi.org/10.1126/science.aar2131>, PMID: 29622724
- Ransick A**, Lindström NO, Liu J, Zhu Q, Guo JJ, Alvarado GF, Kim AD, Black HG, Kim J, McMahon AP. 2019. Single-Cell profiling reveals sex, lineage, and regional diversity in the mouse kidney. *Developmental Cell* **51**:399–413. DOI: <https://doi.org/10.1016/j.devcel.2019.10.005>, PMID: 31689386
- Reginensi A**, Clarkson M, Neirijnck Y, Lu B, Ohyama T, Groves AK, Sock E, Wegner M, Costantini F, Chaboissier M-C, Schedl A. 2011. SOX9 controls epithelial branching by activating RET effector genes during kidney development. *Human Molecular Genetics* **20**:1143–1153. DOI: <https://doi.org/10.1093/hmg/ddq558>
- Ren J**, Rudemiller NP, Wen Y, Lu X, Privratsky JR, Crowley SD. 2020. The transcription factor Twist1 in the distal nephron but not in macrophages nepropagates aristolochic acid nephropathy. *Kidney International* **97**:119–129. DOI: <https://doi.org/10.1016/j.kint.2019.07.016>, PMID: 31685313
- Roche KC**, Gracz AD, Liu XF, Newton V, Akiyama H, Magness ST. 2015. SOX9 maintains reserve stem cells and preserves radioresistance in mouse small intestine. *Gastroenterology* **149**:1553–1563. DOI: <https://doi.org/10.1053/j.gastro.2015.07.004>, PMID: 26170137
- Rudman-Melnick V**, Adam M, Potter A, Chokshi SM, Ma Q, Drake KA, Schuh MP, Kofron JM, Devarajan P, Potter SS. 2020. Single-Cell profiling of AKI in a murine model reveals novel transcriptional signatures, profibrotic phenotype, and Epithelial-to-Stromal crosstalk. *Journal of the American Society of Nephrology* **31**:2793–2814. DOI: <https://doi.org/10.1681/ASN.2020010052>, PMID: 33115917
- Stewart BJ**, Ferdinand JR, Young MD, Mitchell TJ, Loudon KW, Riding AM, Richoz N, Frazer GL, Staniforth JUL, Vieira Braga FA, Botting RA, Popescu DM, Vento-Tormo R, Stephenson E, Cagan A, Farndon SJ, Polanski K, Efremova M, Green K, Del Castillo Velasco-Herrera M, et al. 2019. Spatiotemporal immune zonation of the human kidney. *Science* **365**:1461–1466. DOI: <https://doi.org/10.1126/science.aat5031>, PMID: 31604275
- Stockwell BR**, Friedmann Angeli JP, Bayir H, Bush AI, Conrad M, Dixon SJ, Fulda S, Gascón S, Hatzios SK, Kagan VE, Noel K, Jiang X, Linkermann A, Murphy ME, Overholtzer M, Oyagi A, Pagnussat GC, Park J, Ran Q, Rosenfeld CS, et al. 2017. Ferroptosis: a regulated cell death nexus linking metabolism, redox biology, and disease. *Cell* **171**:273–285. DOI: <https://doi.org/10.1016/j.cell.2017.09.021>, PMID: 28985560
- Strausser SA**, Nakano D, Souma T. 2018. Acute kidney injury to chronic kidney disease transition: insufficient cellular stress response. *Current Opinion in Nephrology and Hypertension* **27**:314–322. DOI: <https://doi.org/10.1097/MNH.0000000000000424>, PMID: 29702491
- Strunz M**, Simon LM, Ansari M, Kathiriya JJ, Angelidis I, Mayr CH, Tsidiridis G, Lange M, Mattner LF, Yee M, Ogar P, Sengupta A, Kukhtevich I, Schneider R, Zhao Z, Voss C, Stoeger T, Neumann JHL, Hilgendorff A, Behr J, et al. 2020. Alveolar regeneration through a Krt8+ transitional stem cell state that persists in human lung fibrosis. *Nature Communications* **11**:3559. DOI: <https://doi.org/10.1038/s41467-020-17358-3>, PMID: 32678092
- Stuart T**, Butler A, Hoffman P, Hafemeister C, Papalexi E, Mauck WM, Hao Y, Stoeckius M, Smibert P, Satija R. 2019. Comprehensive integration of Single-Cell data. *Cell* **177**:1888–1902. DOI: <https://doi.org/10.1016/j.cell.2019.05.031>, PMID: 31178118
- Tata A**, Kobayashi Y, Chow RD, Tran J, Desai A, Massri AJ, McCord TJ, Gunn MD, Tata PR. 2018. Myoepithelial cells of submucosal glands can function as reserve stem cells to regenerate airways after injury. *Cell Stem Cell* **22**:668–683. DOI: <https://doi.org/10.1016/j.stem.2018.03.018>, PMID: 29656943
- Tiwari N**, Tiwari VK, Waldmeier L, Balwierz PJ, Arnold P, Pachkov M, Meyer-Schaller N, Schübeler D, van Nimwegen E, Christofori G. 2013. Sox4 is a master regulator of epithelial-mesenchymal transition by controlling Ezh2 expression and epigenetic reprogramming. *Cancer Cell* **23**:768–783. DOI: <https://doi.org/10.1016/j.ccr.2013.04.020>, PMID: 23764001
- Trapnell C**, Cacchiarelli D, Grimsby J, Pokharel P, Li S, Morse M, Lennon NJ, Livak KJ, Mikkelsen TS, Rinn JL. 2014. The dynamics and regulators of cell fate decisions are revealed by pseudotemporal ordering of single cells. *Nature Biotechnology* **32**:381–386. DOI: <https://doi.org/10.1038/nbt.2859>, PMID: 24658644
- Wenzel SE**, Tyurina YY, Zhao J, St Croix CM, Dar HH, Mao G, Tyurin VA, Anthonymuthu TS, Kapralov AA, Amoscato AA, Mikulska-Ruminska K, Shrivastava IH, Kenny EM, Yang Q, Rosenbaum JC, Sparvero LJ, Emler DR, Wen X, Minami Y, Qu F, et al. 2017. PEBP1 wards ferroptosis by enabling lipoxigenase generation of lipid death signals. *Cell* **171**:628–641. DOI: <https://doi.org/10.1016/j.cell.2017.09.044>, PMID: 29053969
- Wilson PC**, Wu H, Kirita Y, Uchimura K, Ledru N, Rennke HG, Welling PA, Waikar SS, Humphreys BD. 2019. The single-cell transcriptomic landscape of early human diabetic nephropathy. *PNAS* **116**:19619–19625. DOI: <https://doi.org/10.1073/pnas.1908706116>
- Witzgall R**, Brown D, Schwarz C, Bonventre JV. 1994. Localization of proliferating cell nuclear antigen, Vimentin, c-Fos, and clusterin in the postischemic kidney evidence for a heterogenous genetic response among nephron segments, and a large pool of mitotically active and dedifferentiated cells. *Journal of Clinical Investigation* **93**:2175–2188. DOI: <https://doi.org/10.1172/JCI117214>, PMID: 7910173
- Yang WS**, SriRamaratnam R, Welsch ME, Shimada K, Skouta R, Viswanathan VS, Cheah JH, Clemons PA, Shamji AF, Clish CB, Brown LM, Girotti AW, Cornish VW, Schreiber SL, Stockwell BR. 2014. Regulation of ferroptotic

- Cancer cell death by GPX4. *Cell* **156**:317–331. DOI: <https://doi.org/10.1016/j.cell.2013.12.010>, PMID: 24439385
- Yoo SE**, Chen L, Na R, Liu Y, Rios C, Van Remmen H, Richardson A, Ran Q. 2012. Gpx4 ablation in adult mice results in a lethal phenotype accompanied by neuronal loss in brain. *Free Radical Biology and Medicine* **52**:1820–1827. DOI: <https://doi.org/10.1016/j.freeradbiomed.2012.02.043>, PMID: 22401858
- Yuan H**, Li X, Zhang X, Kang R, Tang D. 2016. Identification of ACSL4 as a biomarker and contributor of ferroptosis. *Biochemical and Biophysical Research Communications* **478**:1338–1343. DOI: <https://doi.org/10.1016/j.bbrc.2016.08.124>, PMID: 27565726
- Zhao Z**, Wu J, Xu H, Zhou C, Han B, Zhu H, Hu Z, Ma Z, Ming Z, Yao Y, Zeng R, Xu G. 2020. XJB-5-131 inhibited ferroptosis in tubular epithelial cells after ischemia-reperfusion injury. *Cell Death & Disease* **11**:629. DOI: <https://doi.org/10.1038/s41419-020-02871-6>, PMID: 32796819